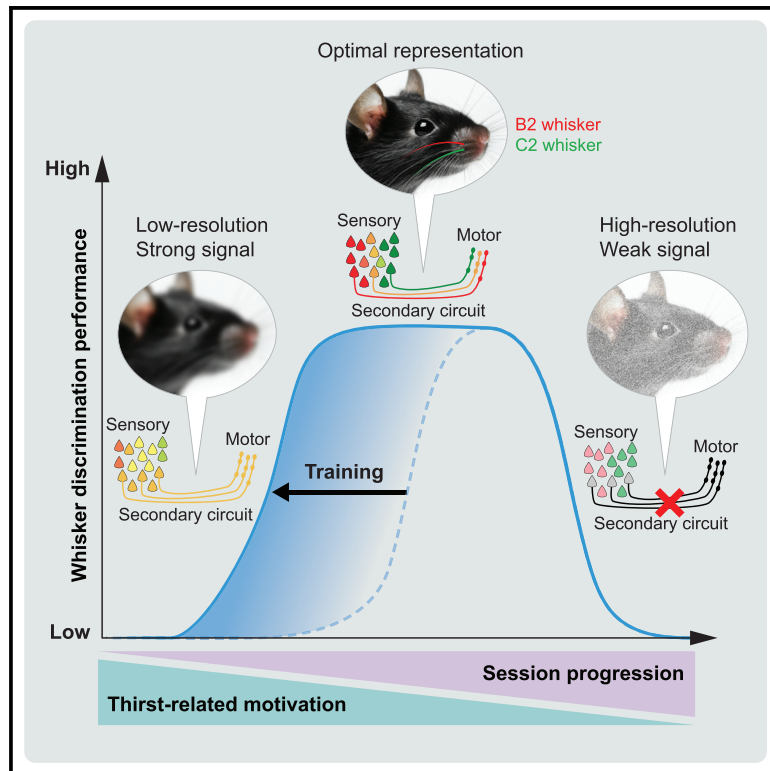


Cortical sensory processing across motivational states during goal-directed behavior

Graphical abstract



Authors

Giulio Matteucci, Maëlle Guyoton, Johannes M. Mayrhofer, Matthieu Auffret, Georgios Foustoukos, Carl C.H. Petersen, Sami El-Boustani

Correspondence

carl.petersen@epfl.ch (C.C.H.P.), sami.el-boustani@unige.ch (S.E.-B.)

In brief

Perceptual decision-making is studied in water-restricted mice to motivate task performance. It is unclear how thirst-induced motivation affects learning and perception. Matteucci et al. revealed that sensory encoding of whisker sensation is impaired in low or high motivation regimes and improves as mice learn to better control their motivational state.

Highlights

- wS1-wS2-wM2 cortical pathway is involved in a two-whisker discrimination task
- Selectivity to sensory and motor events increases along this sensorimotor pathway
- Improved performance is explained by changes in thirst-related motivational states
- Sensory decoding of whisker identity in wS2-wM2 correlates with task performance



Article

Cortical sensory processing across motivational states during goal-directed behavior

Giulio Matteucci,¹ Maëlle Guyoton,¹ Johannes M. Mayrhofer,² Matthieu Auffret,² Georgios Foustoukos,² Carl C.H. Petersen,^{2,*} and Sami El-Boustani^{1,2,3,*}

¹Department of Basic Neurosciences, Faculty of Medicine, University of Geneva, 1 Rue Michel-Servet, 1206 Geneva, Switzerland

²Laboratory of Sensory Processing, Brain Mind Institute, Faculty of Life Sciences, Ecole Polytechnique Fédérale de Lausanne (EPFL), EPFL-SV-BMI-LSSENS Station 19, CH-1015 Lausanne, Switzerland

³Lead contact

*Correspondence: carl.petersen@epfl.ch (C.C.H.P.), sami.el-boustani@unige.ch (S.E.-B.)

<https://doi.org/10.1016/j.neuron.2022.09.032>

SUMMARY

Behavioral states can influence performance of goal-directed sensorimotor tasks. Yet, it is unclear how altered neuronal sensory representations in these states relate to task performance and learning. We trained water-restricted mice in a two-whisker discrimination task to study cortical circuits underlying perceptual decision-making under different levels of thirst. We identified somatosensory cortices as well as the premotor cortex as part of the circuit necessary for task execution. Two-photon calcium imaging in these areas identified populations selective to sensory or motor events. Analysis of task performance during individual sessions revealed distinct behavioral states induced by decreasing levels of thirst-related motivation. Learning was better explained by improvements in motivational state control rather than sensorimotor association. Whisker sensory representations in the cortex were altered across behavioral states. In particular, whisker stimuli could be better decoded from neuronal activity during high task performance states, suggesting that state-dependent changes of sensory processing influence decision-making.

INTRODUCTION

Perceptual decision-making is expressed through sensorimotor transformations: sensory-evoked responses in the brain are transformed into motor plans guiding execution of an appropriate action. Brain circuits involved in this behavior have long been studied in primates (Parker and Newsome, 1998; Romo and Rossi-Pool, 2020). However, access to micro-circuits is challenging in these animals. The mouse model has become increasingly promising for more advanced recording techniques relying on genetic tools for circuit interrogation (Chen et al., 2013b; Fenno et al., 2011; Kim and Schnitzer, 2022). Head-fixed mice can be trained to perform behavioral tasks based on visual (Burgess et al., 2016; Goltstein et al., 2021; Steinmetz et al., 2019), olfactory (Allen et al., 2017; Komiyama et al., 2010), tactile (Chen et al., 2013a; Guo et al., 2014; Harrell et al., 2021; Sachidanandam et al., 2013), or auditory (Kuchibhotla et al., 2017; Pinto and Dan, 2015; Xin et al., 2019) sensory cues.

Sensory processing is strongly modulated by ongoing behavioral states that might vary during task execution. Exploratory behaviors such as locomotion or whisking can modulate the amplitude of evoked sensory responses (Ayaz et al., 2013; Crochet and Petersen, 2006; Ferezou et al., 2007; Gasselini et al., 2021; Szwed et al., 2003; Vinck et al., 2015). Task engagement and arousal have also been shown to enhance

sensory responses during goal-directed behaviors (Kuchibhotla et al., 2017; Lee et al., 2020; McGinley et al., 2015). More importantly, appetitive-related states that are used to motivate behavior in these tasks can strongly alter brain-wide activity and sensory representations across the brain (Allen et al., 2019; Burgess et al., 2016; Henschke et al., 2020; Livneh et al., 2017, 2020). How thirst-related motivational states can alter sensory processing in relation to task performance remains unclear.

In mice, the whisker somatosensory system is prominent, as rodents rely on their whiskers to explore their environment, measure distances, guide locomotion, and identify objects (Grant and Goss, 2022). Recent studies have investigated whisker perception with simple detection tasks in which water-restricted mice have to produce an action to obtain water upon whisker stimulation (Kwon et al., 2016; Le Merre et al., 2018; Sachidanandam et al., 2013), revealing the existence of decision-modulated sensory signals in somatosensory cortices (Kwon et al., 2016; Yamashita and Petersen, 2016; Yang et al., 2016) and in some thalamocortical projections (El-Boustani et al., 2020). However, because of widespread representations of multiple behavior-related variables in the cortex (Musall et al., 2019; Steinmetz et al., 2019; Stringer et al., 2019), it has been challenging to fully understand the nature of sensory processing during task performance.



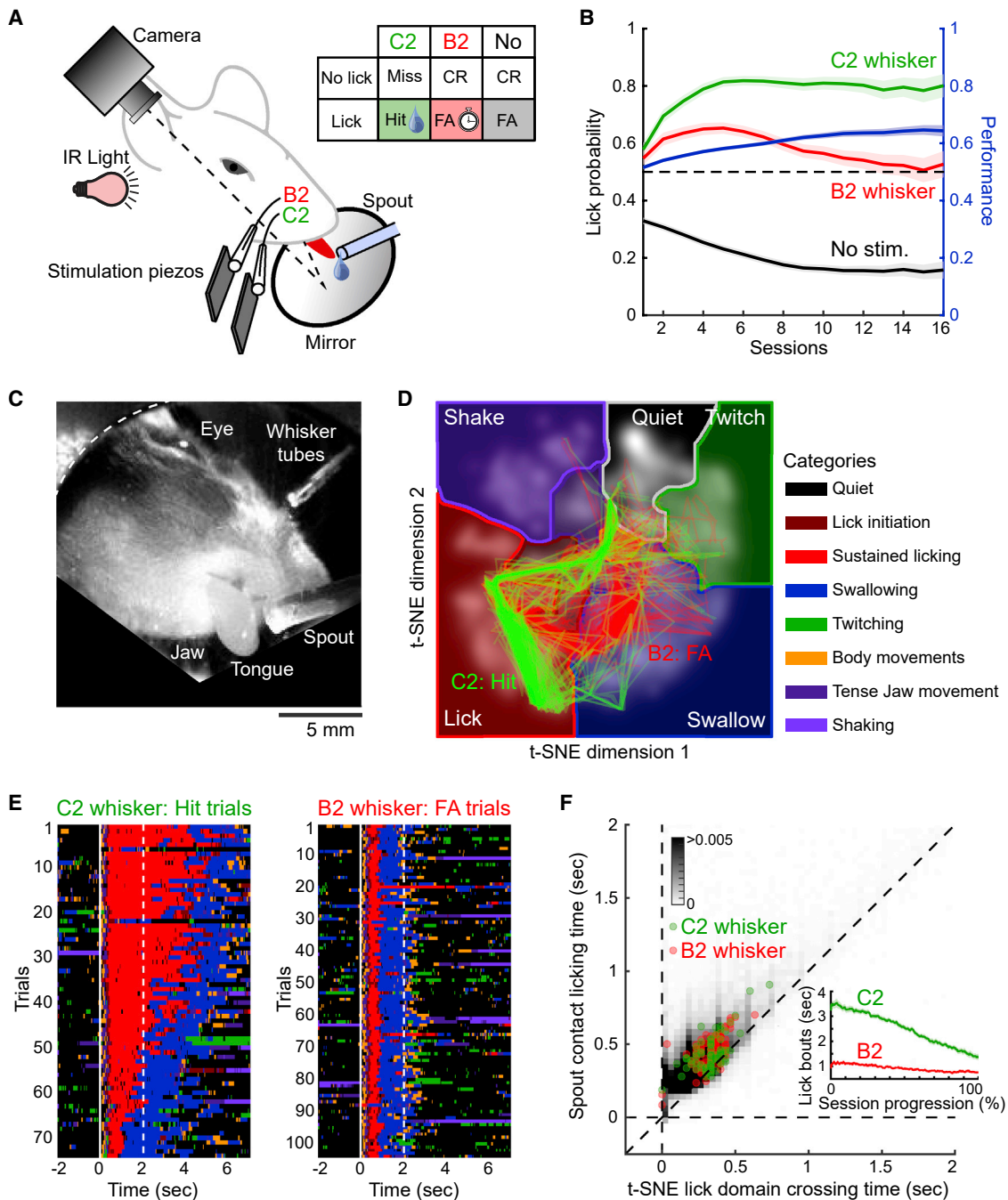


Figure 1. Head-fixed mice can learn a two-whisker discrimination task with distinct orofacial responses

(A) Schematic of the experimental design. The table represents outcomes (Hit, False alarm [FA], Miss, or Correct rejection [CR]) for each combination of stimulus condition (C2 whisker, B2 whisker, No stimulus) and mouse action (lick or no lick).

(B) Lick probability for all stimulus conditions across sessions and averaged over mice ($N = 92$ mice). Whisker discrimination performance is shown with the right y-axis (blue). Dashed black line: chance level. Shaded areas: SEM.

(C) Snapshot from the camera filming the face of the mouse.

(D) Trajectories in the t-SNE space corresponding to a single session for Hit (green) and FA (red) trials. Trajectories start at stimulus onset and end after the response window (2 s). Domains for specific orofacial movements are highlighted with colors and labeled (see Figure S1A for examples of Miss and CR trajectories).

(E) Ethograms based on the t-SNE in (D) for all Hit and FA trials in chronological order. Colors correspond to state location at each time point with the same color code as in (D). The white line indicates stimulus onset and the dashed white line indicates the end of the response window (see Figure S1B for examples of Miss and CR ethograms).

(legend continued on next page)

RESULTS

Head-fixed mice can learn a two-whisker discrimination task with distinct orofacial responses

To address this issue, we developed a go/no go two-whisker discrimination task for head-fixed mice under a water-restriction schedule to investigate sensory and motor representations during perceptual decision-making in different behavioral states. Mice were head-fixed in the dark and received short pulsatile tactile stimulations on one of two neighboring whiskers: the C2 or the B2 whisker (Figure 1A). Licking a spout in response to C2 whisker stimuli (Go) within a 2 s window following stimulus onset delivered a drop of water reward from the spout (Hit trials), whereas licking in response to the B2 whisker (No go) resulted in a 10 s long timeout (False Alarm trials). This two-whisker discrimination task is more challenging than simpler whisker detection tasks, as it requires mice to make perceptual decisions based on neighboring whiskers that share overlapping cortical representations. During the first days of training, mice quickly learned to lick in response to whisker stimulation but displayed little discrimination between the two whiskers (Figure 1B). After the second week of training, mice displayed a significantly higher lick probability for C2 whisker than for B2 whisker stimulation (Figure 1B, see STAR Methods).

To tease apart motor and sensory signals from neural activity, it is critical to precisely describe motor responses to accurately estimate reaction times as the earliest detectable orofacial movements for licking. While licking behavior during execution of the task was monitored through vibrations on the spout, precise lick reaction times were obtained by offline analysis of orofacial movements filmed during each trial (Figures 1A and 1C). The movies were analyzed, adapting a method for non-linear dimensional reduction previously used to classify stereotyped motor behaviors of flies (Berman et al., 2014). This method is based on the t-distributed stochastic neighbor embedding algorithm (t-SNE) (Van Der Maaten and Hinton, 2008) (see STAR Methods). In the resulting two-dimensional t-SNE space, individual trials could be represented as trajectories traversing domains corresponding to stereotypical orofacial movements (Figures 1D and S1A). Some categories of orofacial movements were clearly identified in all mice and all sessions: lick initiation, sustained licking, swallowing, twitching, tense jaw movement, shaking, and body movements (Video S1).

This parcellation of the t-SNE space could be used to represent sessions as ethograms describing the sequence of actions performed by mice in Hit or False Alarm trials (Figure 1E). In these trials, mice produced an initial lick upon whisker stimulation followed by sustained licking and swallowing when a reward was available (Hit trials), whereas mice quickly resumed the quiet state if no reward was delivered (False Alarm trials) (Videos S2 and S3). The t-SNE representation could be used to estimate licking reaction times more accurately than what was estimated

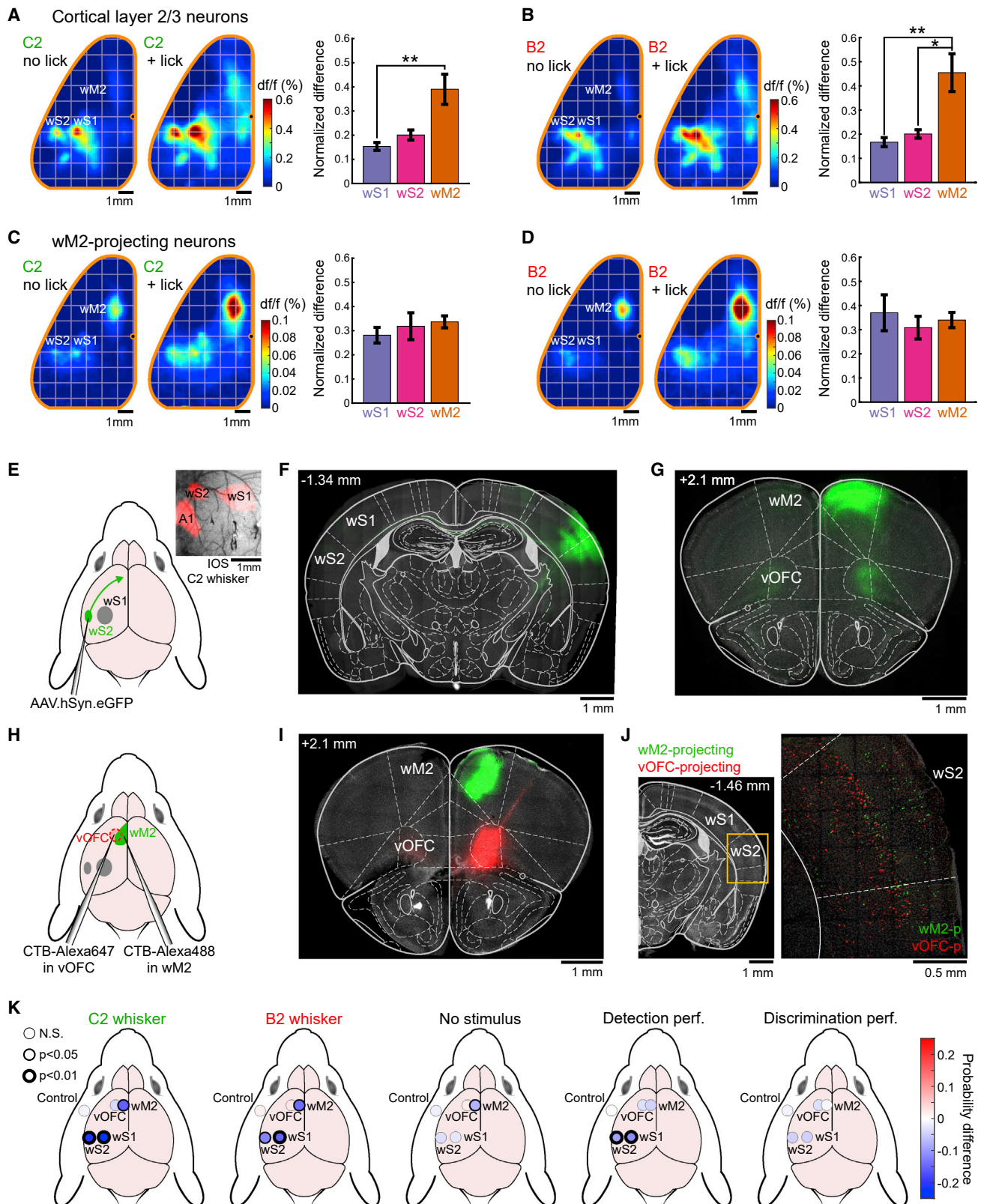
by detecting spout vibrations. We defined the t-SNE reaction time as the first frame where the lick domain is crossed by the trajectory in each lick trial (Figure 1D, see STAR Methods). This definition of the reaction time correlated well with the values obtained based on spout contact detection but with shorter latencies (Figure 1F). Orofacial ethograms also revealed that mice produced decreasing bouts of sustained licking in response to water reward as the session progressed. Indeed, licking bout duration linearly decreased with each reward until it almost reached the level of licking activity observed during unrewarded trials (Figure 1F, inset). This stereotypical decay of licking bout duration during individual sessions indicated changes in thirst-related motivational state. Mice licked continuously for several seconds when thirsty (at the beginning of the session) and licked only once when completely satiated (at the end of the session).

The secondary whisker sensorimotor pathway contributes to task execution

To identify cortical regions involved in the execution of the task, we first performed wide-field calcium imaging over the dorsal cortex of head-fixed mice. Transgenic mice (Daigle et al., 2018) expressing the genetically encoded calcium indicator GCaMP6f in cortical layers 2/3 (see STAR Methods) were trained in the task. Functional maps for each trial type were averaged over several sessions and then compared across mice (Figures 2A and S2A). Upon C2 whisker stimulation, the primary and secondary whisker somatosensory cortices (wS1 and wS2) were activated almost simultaneously, as previously reported (Esmaeili et al., 2021). In trials where mice did not lick in response to the whisker stimulus, this pattern of activity was maintained transiently and then decayed to baseline activity. However, when mice decided to lick, we observed over the same time window (0.12 to 0.18 s, preceding the average lick reaction time of 0.28 s) a strong activation of the premotor cortex wM2, known to be involved in whisker-based goal-directed sensorimotor transformation (Esmaeili et al., 2021, 2022; Gilad et al., 2018). The same was true for B2 whisker stimuli, though with activity in different somatotopic locations in wS1 and wS2 (Figure 2B and S2A).

As the premotor cortex is known to be involved in action selection during decision-making (Barthas and Kwan, 2017; Sul et al., 2011), we investigated whether somatosensory cortex might contribute to driving activity in this area. We performed the same wide-field imaging experiments to measure GCaMP6f activity in wM2-projecting neurons (see STAR Methods). Upon whisker stimulation, we observed that only wS1 and wS2 responded prior to wM2, indicating that these sensory areas could directly be driving activity in wM2 (Figures 2C, 2D, and S2B). Interestingly, we found a comparable enhancement of activity between the retrogradely labeled neurons in somatosensory cortices wS1/wS2 and premotor cortex wM2 in lick trials

(F) Comparison of first lick reaction times measured with spout contact or based on t-SNE lick domain crossing. Trials corresponding to the session (D–E) are shown for C2 (green) and B2 (red) whisker. The gray scale map represents the density plots for all lick trials ($n = 50,879$ trials) across all mice ($N = 27$) and sessions ($n = 346$). Average reaction time across all mice: 0.280 ± 0.001 s (t-SNE) versus 0.420 ± 0.001 s (spout), two-sided paired t test, $p = 2 \times 10^{-307}$. Inset: average lick bout duration evoked by C2 or B2 whisker stimulation across all sessions of all mice ($n = 346$ sessions, $N = 27$ mice) as a function of session progression (see STAR Methods). Shaded areas: SEM.



(legend on next page)

(Figures 2C and 2D, Kruskal-Wallis one-way ANOVA test, $p = 0.22$ for C2 and $p = 0.55$ for B2).

Given that frontal projections from wS1 primarily project to wM1 (Yamashita et al., 2018), we performed anatomical tracing experiments to investigate whether wM2 might receive direct projections from wS2. We expressed eGFP in wS2 neurons through viral vector injection (Figures 2E and 2F). We found strong axonal projections of wS2 neurons in wM2 but also in the ventral orbitofrontal cortex (vOFC) (Figure 2G). To identify the locations of projecting neurons in wS2, we injected the retrograde marker cholera toxin subunit B (CTB) in these target areas. We used CTB conjugated with two different Alexa dyes for wM2 and vOFC to separately label wM2-projecting and vOFC-projecting neurons (Figures 2H and 2I). We found large populations of neurons projecting to these two frontal structures in wS2 (Figure 2J) with very little overlap (5.7% of 669 wM2-projecting neurons and 9.5% of 400 vOFC-projecting neurons, $N = 2$ mice). These neurons were found in superficial and deep layers, but not in layer 4. These results are in line with previous studies showing that motor cortices receive direct inputs from somatosensory cortices (Esmaeili et al., 2022), whereas the adjacent anterior cingulate cortex receives predominant inputs from visual cortices (Zhang et al., 2016).

To test whether these cortical regions are involved in the whisker-based sensorimotor transformation, we used optogenetics to inactivate these areas during execution of the task. We expressed a Cre-dependent version of the light-gated chloride channel iC^{++} (Berndt et al., 2016) in $Emx1$ -Cre mice through viral vector injections. Mice performed the task while we inactivated wS1, wS2, wM2, vOFC, or a control area with no expression in a subset of trials (Figures 2K and S3, see STAR Methods). We performed unilateral inactivation, as previous studies have shown that the performance of whisker-based sensorimotor tasks is strongly impaired when the contralateral hemisphere is inactivated during sensory stimulation (Esmaeili et al., 2021; Guo et al., 2014). We do not exclude that callosal connections could provide inputs to the ipsilateral hemisphere, but we think these signals would likely contribute to a lesser extent.

In trials in which a whisker was stimulated, inactivation of wS1, wS2, and wM2 reduced licking probability, whereas inactivation of vOFC or the control area had no effect on the licking behavior. During trials without any whisker stimulation, only wM2 inactivation significantly reduced licking probability. As a consequence, wS1 and wS2 inactivation resulted in a significant drop in whisker detection performance. On the contrary, inactivation of wM2 did not affect whisker detection performance, as licking was reduced regardless of the stimulation condition. This result indicates a change of function between wS1/wS2 and wM2, with the former areas being involved in whisker perception and the latter area being involved in motor planning for licking. Because licking probability was reduced equally for both whiskers, none of these inactivation experiments affected the discrimination performance. Note that inactivation of these areas affects downstream subcortical regions and further optogenetic dissections would be required to characterize circuits for sensorimotor transformation beyond cortical regions. Altogether, these results show that the wS1-wS2-wM2 pathway is involved in the execution of the task.

Sensory neurons in deep layers of the secondary sensorimotor pathway show strong response modulation preceding licking

To study sensory and motor representations in these areas at the cellular level we performed two-photon calcium imaging experiments. We used a cranial window-microprism assembly to image cortical responses across layers (Figure 3A) and to access projecting neurons in deep layers. Expression of genetically encoded calcium indicators in these areas was obtained through different strategies combining viral vector injections with retrograde or transsynaptic anterograde transduction properties in transgenic mouse lines (see STAR Methods). During passive C2 or B2 whisker stimulation, we observed that these neuronal populations displayed different spatial organizations and degrees of whisker selectivity (Figure 3B). wS1 was characterized by a clear delimitation between neurons responding to C2 and the nearby B2 whisker, reflecting the somatotopic organization of the barrel cortex. Functional organization was not so clear in other neuronal populations.

Figure 2. The secondary whisker sensorimotor pathway contributes to task execution

(A) Wide-field average calcium response over the dorsal cortex of mice expressing GCaMP6f in cortical layers 2/3 during C2 whisker stimulation (left: without licking, middle: with licking). The maps are obtained by averaging across mice ($N = 11$ mice) and over a 60 ms time window preceding lick-related widespread activity (see Figure S2A). Right panel: normalized difference between the no-lick and lick conditions for wS1, wS2, and wM2 (Kruskal-Wallis test with Bonferroni correction, $*p < 0.05$, $**p < 0.01$). Grid size: 1 mm. Orange outline indicates limit of the imaged dorsal cortex and the orange dot indicates bregma.

(B) Same as (A) for B2 whisker stimulation.

(C) Same as (A) but for mice expressing GCaMP6f only in wM2-projecting neurons throughout the dorsal cortex ($N = 4$ mice, see Figure S2B). We found no significant differences between areas (Kruskal-Wallis one-way ANOVA test, $p = 0.22$).

(D) Same as (C) for B2 whisker stimulation (Kruskal-Wallis one-way ANOVA test, $p = 0.55$).

(E) Schematic of the injection of AAV.hSyn.eGFP in wS2. Inset: Optical intrinsic signal imaged over the surface of the skull used to localize wS2 for viral vector injection.

(F) Coronal brain slice at the level of the injection site.

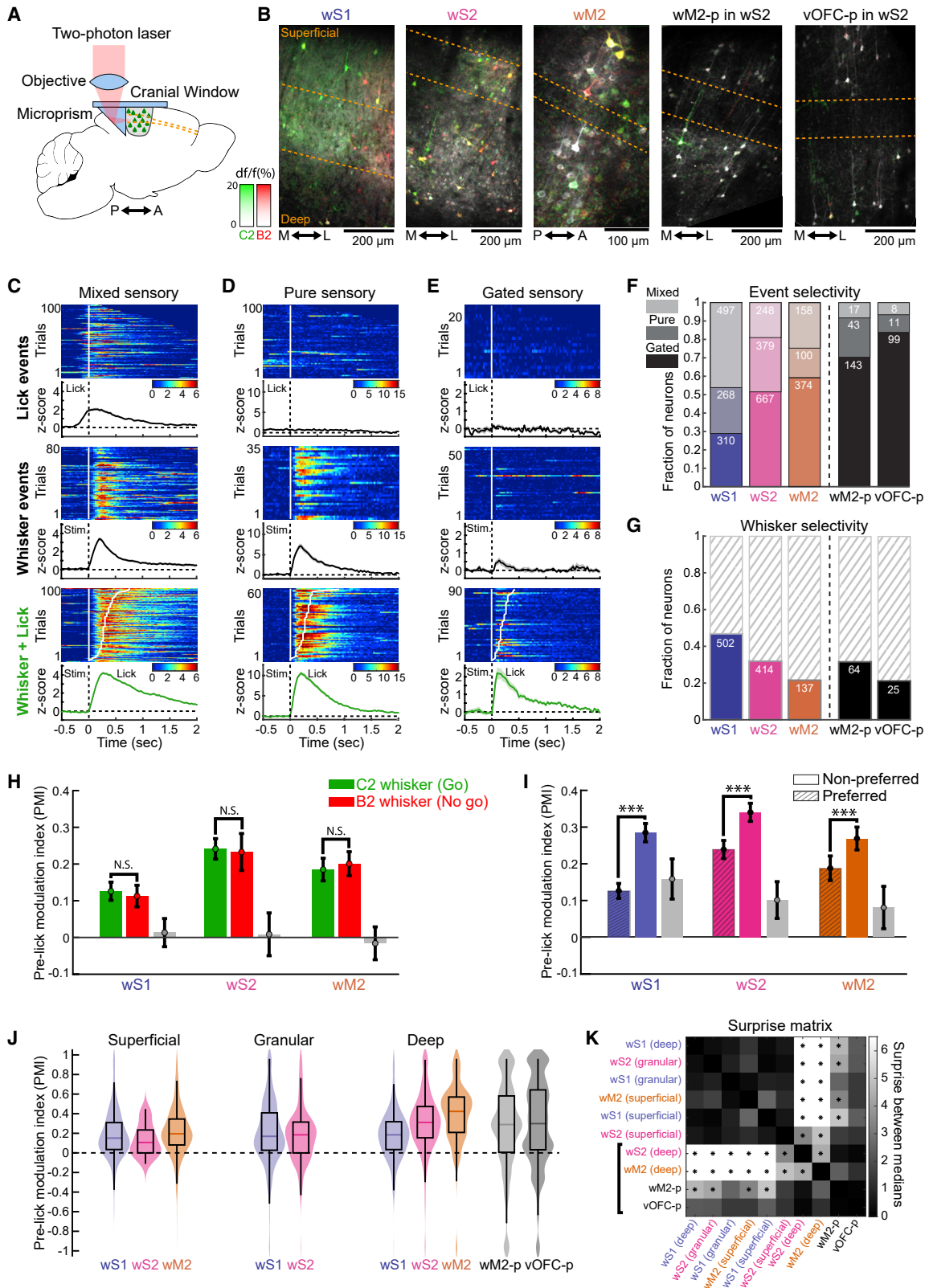
(G) Coronal slice from the same brain in (F) with axonal projection of wS2 neurons in wM2 and vOFC.

(H) Schematic of the injection of CTB-Alexa647 in vOFC and CTB-Alexa488 in wM2 for retrograde labeling of cortico-cortical projecting neurons in wS2.

(I) Coronal brain slice at the level of the injection sites with CTB-Alexa647 (red) and CTB-Alexa488 (green).

(J) Coronal slice from the same brain in (I) with wM2 and vOFC projecting neurons in wS2. In (F), (G), (I), and (J) reference atlas (Paxinos and Franklin, 2000) with anterior-posterior locations relative to bregma is overlaid on top of the image.

(K) Effect of optogenetic silencing of specific areas on lick probability and performance. Color for each location indicates difference in probability between trials with and without light (see Figure S3). Line thickness indicates significance (two-sided paired Wilcoxon test, thin: $p > 0.05$, medium: $0.01 < p < 0.05$, and thick: $p < 0.01$). Average for each area was performed over several mice: wS1 ($N = 10$ mice), wS2 ($N = 10$ mice), wM2 ($N = 7$ mice), vOFC ($N = 8$ mice), and Control ($N = 11$ mice).



(legend on next page)

Among all neurons we imaged, we observed distinct populations of neurons responding to whisker stimulation and/or motor-related events (see [STAR Methods](#)). We first focused on neurons that displayed whisker-related sensory responses (wS1: 58%, $n = 1,864$; wS2: 36%, $n = 3,578$; wM2: 41%, $n = 1,525$; wM2-p in wS2: 38%, $n = 530$; vOFC-p in wS2: 29%, $n = 401$ of task-responsive neurons, with the remaining neurons being exclusively responsive to motor-related events). We identified three types of sensory neurons displaying different forms of event selectivity ([Figure S4A](#)). “Mixed sensory” neurons responded to whisker stimuli in absence of licking but responded also to lick events in absence of whisker stimulation ([Figure 3C](#)). “Pure sensory” neurons responded to whisker stimulation alone but not to isolated lick events. Responses of these neurons to whisker stimuli during lick trials could, however, be strongly enhanced even before licking ([Figure 3D](#)). “Gated sensory” neurons did not respond to whisker stimuli alone or to lick events alone but did respond strongly to whisker stimuli in lick trials ([Figure 3E](#)). Responses of these neurons during lick trials preceded licking events and were not time-locked to them, indicating a sensory signal rather than a motor one (see [STAR Methods](#)). Indeed, the response latency or peak of these neurons did not scale with increasing reaction times, a property expected for motor planning neurons. These neurons could be considered an extreme case of pure sensory neurons with high lick-related response enhancement, though we found that their modulation during licking was significantly stronger than pure sensory neurons, and, therefore, gated sensory neurons constitute a distinct population of sensory neurons ([Figure S4B](#)).

Comparing the distribution of these cell types in all neuronal populations, we found that half of the neurons in wS1 were mixed and showed poor event selectivity. In contrast, wS2 and wM2

were dominated by gated sensory neurons with projecting neurons in wS2 containing a large majority of gated neurons ([Figure 3F](#)). Thus, we observed increasing event selectivity along the wS1-wS2-wM2 pathway. Note that the bulk layer 2/3 wide-field signal modulation that we observed in wS1 and wS2 during lick trials ([Figures 2A–2D](#)) appears to originate from different single-cell response properties with overlapping (wS1) or distinct (wS2) representations of sensory and motor events. Whisker selectivity along the same pathway was decreasing ([Figure 3G](#)). Interestingly, the functional properties of neurons in wS1 and wS2 reflected the event selectivity found in the thalamocortical projections innervating these areas ([El-Boustani et al., 2020](#)).

How are whisker-evoked responses related to the decision to lick? Previous studies have tried to identify decision-related activity in sensory cortices by comparing sensory evoked responses during lick and no-lick trials ([Kwon et al., 2016](#); [Takahashi et al., 2016](#); [Yamashita and Petersen, 2016](#); [Yang et al., 2016](#)). As motor-related signals are widespread in the cortex and can contaminate sensory signals upon licking, we defined a modulation index to compare lick and no-lick conditions before licking happened based on the t-SNE reaction time: the pre-lick modulation index (PMI). This index compares whisker responses during individual lick trials to the average whisker response in the absence of licking in time windows preceding licking (see [STAR Methods](#) and [Figure S4C](#)). We first investigated task-specific modulation of whisker representations. In this scenario, responses to C2 or B2 whisker stimulation would be differently modulated, as they have different behavioral relevance in this task (C2 being associated to a reward and B2 to a timeout punishment). This modulation could be the result of top-down selective modulations. When comparing response modulation between C2 and B2, we found no significant differences in any of

Figure 3. Sensory neurons in deep layers of the secondary sensorimotor pathway show strong response modulation preceding licking

- (A) Schematic of two-photon calcium imaging of cortical neurons through a microp prism-cranial window assembly.
- (B) Example field-of-views imaged through the microp prism for different cortical populations. The color maps overlaid represent the maximum calcium response to C2 (green) or B2 (red) whisker stimulation in no-lick trials. Boundaries between layers are indicated with dashed orange lines. M, medial; L, lateral; P, posterior; and A, anterior.
- (C) Example “mixed sensory” neuron. Top: Plots showing Z scored calcium responses aligned to isolated lick events. Heatmap representing all single-trial responses is above the average response across trials. Shaded area: SEM. Middle: Same plots for calcium responses in Z score aligned to whisker stimulation in the absence of licking. Bottom: Same plots for Z scored calcium responses aligned to whisker stimulation followed by licking. The straight white line indicates timing of the whisker stimulus, and the subsequent white line indicates the timing of first lick for trials ordered by increasing reaction times.
- (D) Same as (C) but for an example “pure sensory” neuron.
- (E) Same as (C) but for an example “gated sensory” neuron.
- (F) Distributions of neurons with mixed, pure, or gated sensory responses across all neuronal populations in (B). Population sizes are indicated in white.
- (G) Proportion of sensory neurons with significant whisker selectivity (see [STAR Methods](#)) across all neuronal populations in (B). Population sizes are indicated in white.
- (H) PMI across all sensory neurons in each population as a function of absolute whisker preference (C2-whisker-preferring in green and B2-whisker-preferring in red, difference in gray). Bar heights represent medians and error bars display 95% confidence intervals obtained from a bootstrap procedure to compare PMI in B2- and C2-preferring populations with matched population sizes (wS1: $n = 366$, wS2: $n = 392$, wM2: $n = 293$, see [STAR Methods](#)). N.S., not significant (bootstrap test, wS1: $p = 0.49897$; wS2: $p = 0.77208$; wM2: $p = 48601$).
- (I) PMI as a function of whisker preference for individual sensory neurons (C2 is preferred if $WSI > 0$ and B2 is preferred if $WSI < 0$). Bars indicating median PMI on preferred whisker are striped, whereas bars indicating median PMI on the non-preferred whisker are plain. Gray bars represent the difference. Error bars display 95% confidence intervals obtained from a two-sample paired median difference test. Neuronal population sizes are matched because each neuron always has a preferred and a non-preferred whisker (wS1: $n = 849$, wS2: $n = 816$, wM2: $n = 816$). *** $p < 0.001$ (Two-sided paired Wilcoxon test, wS1: $p = 3 \times 10^{-30}$; wS2: $p = 1 \times 10^{-15}$; wM2: $p = 2 \times 10^{-8}$).
- (J) PMI across imaged populations and cortical depths. Violin plots represent full distributions of PMI values computed on both C2 and B2 whiskers. Boxplots represent medians, interquartile range, and max/min without outliers (outside 1.5 times interquartile range from 1st and 4th quartile).
- (K) Surprise matrix for median PMI value comparison across all conditions in (J). Surprise values plotted derive from p values obtained with a two-sided paired Wilcoxon test. * $p < 0.05$ with Bonferroni correction. The matrix has been reordered using a hierarchical clustering algorithm (see [STAR Methods](#)). See also [Figure S4](#).

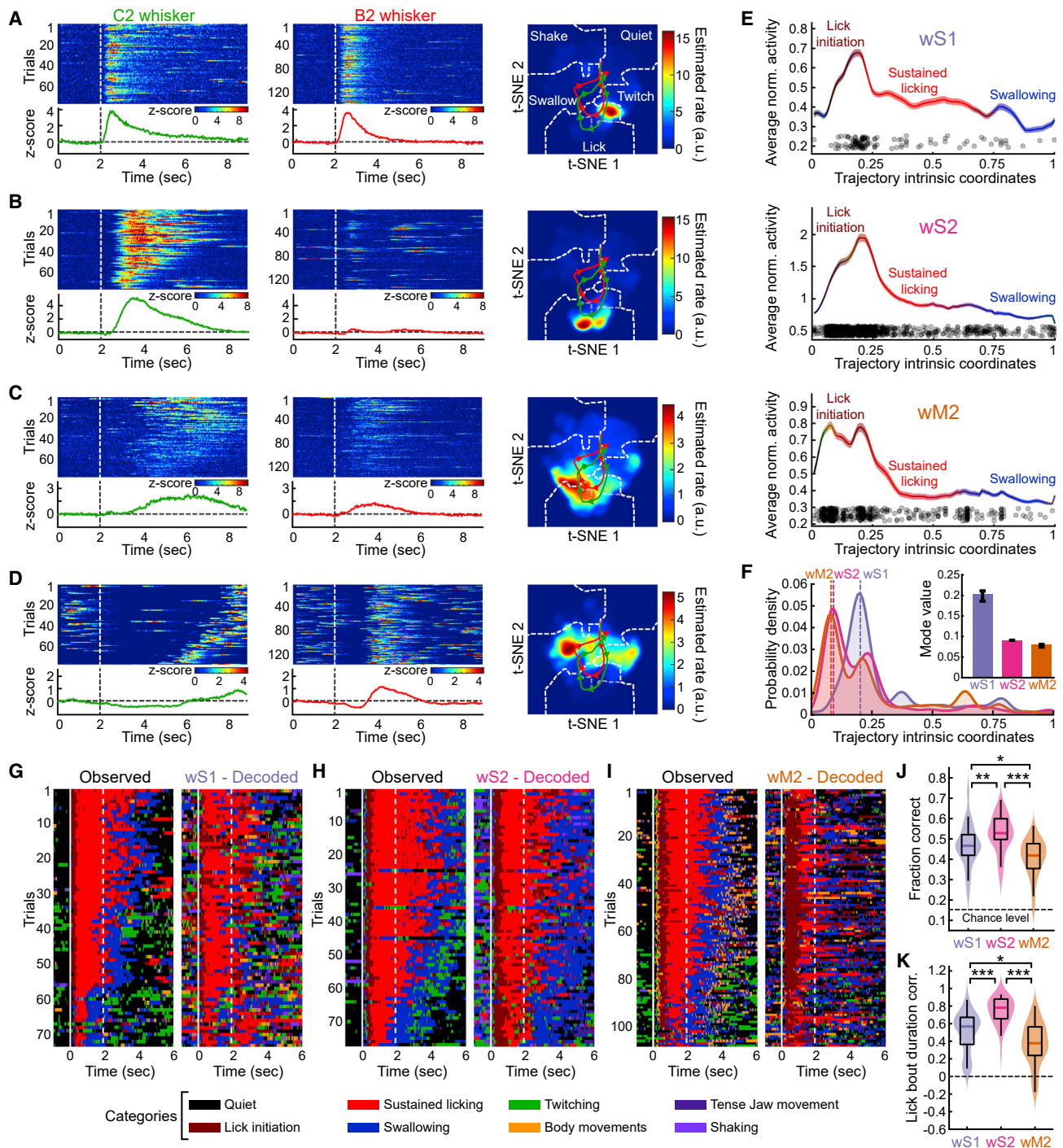


Figure 4. Motor-related neurons in the whisker secondary somatosensory cortex exhibit a rich representation of orofacial movements

(A) Example motor-related neuron in wS2 encoding lick initiation. Left panels show Z scored calcium responses in Hit trials. Heatmap represents chronologically ordered trial responses aligned to stimulus onset (dashed white line). Average response across trials along with SEM is represented below. Middle panels show the same for FA trials. Right panel shows action tuning map of the neuron in the orofacial movement state space (see STAR Methods). Colored lines represent the mode of C2 (green) and B2 (red) lick trial reparametrized trajectories in the orofacial state-space (see STAR Methods).

(B) Same plots for an example motor-related neuron in the same wS2 recording as (A) encoding sustained licking.

(C) Same plots for an example motor-related neuron in the same wS2 recording as (A) encoding transition between sustained licking and swallowing.

(D) Same plots for an example motor-related neuron in the same wS2 recording as (A) encoding swallowing.

(legend continued on next page)

the imaged areas (Figure 3H). However, when modulation was compared in terms of preferred and non-preferred whiskers for each neuron, the PMI was significantly larger for the non-preferred whisker for all populations (Figure 3I). As decisional signals should be independent of the whisker identity when mice decide to lick, this heterogeneous enhancement of sensory responses across whiskers rather indicates an alteration of the sensory representation used to drive decision-making. These strong modulations were more prominent in neurons located in deep cortical layers of the secondary sensorimotor pathway wS2-wM2 and projecting neurons in wS2 (Figure 3J). Cluster analysis of the surprise matrix comparing statistical significance between populations and layers revealed the existence of a network of highly modulated neurons within wS2-wM2 deep layers (Figure 3K).

Motor-related neurons in the whisker secondary somatosensory cortex exhibit a rich representation of orofacial movements

Task-responsive neurons that were not classified as sensory displayed complex patterns of activity during behavioral sessions that correlated with orofacial movements. Movements can trigger widespread activity in the cortex (Musall et al., 2019; Steinmetz et al., 2019; Stringer et al., 2019). To precisely describe the tuning properties of these neurons, we took advantage of the t-SNE representation for orofacial movements (Figure 1D). As mice explored this space during single sessions, we could monitor the activity of single neurons and map out their response patterns in different regions of the t-SNE two-dimensional space. Much alike the mapping of place cells in hippocampal circuits, this allowed us to map the state preference of individual neurons in the t-SNE space (Figures 4A–4D). We referred to these maps as action tuning maps (see STAR Methods). This analysis was performed using neurons that did not have whisker sensory responses to avoid spurious tuning properties in action maps, as passive whisker stimulation could occur independent of ongoing orofacial movements.

We found neurons that responded to specific phases of lick trials with, for instance, tuning for lick initiation (Figure 4A), sus-

tained licking at high pace (Figure 4B), transition between licking and swallowing (Figure 4C), or swallowing (Figure 4D). Distributions of tuning preferences were quite broad and covered trajectories explored during licking. To compare these distributions across areas, we reparametrized trajectories to have a comparable duration from the exit to the re-entrance of the quiet state (see STAR Methods). Distribution of tuning peaks along this trajectory showed that most wM2 neurons were responsive early at lick initiation, shortly followed by wS2 neurons and then wS1 neurons (Figures 4E and 4F). This is in line with a role of wM2 in generating lick motor signals as a result of the decision-making process that could then backpropagate to upstream sensory areas.

As the tuning distribution was rather broad in all areas, we quantified how well orofacial movements could be decoded from these neuronal populations using a Bayesian decoder (see STAR Methods). Decoding was performed on ethograms that we tried to reconstruct from neurons and compare to the ones directly obtained from the t-SNE trajectories (Figures 4G–4I). We observed that wS2 neuronal populations were significantly better than any other population at decoding sequences of orofacial movements (Figure 4J), followed by wS1 and then wM2. The presence of motor-related responses across these cortical regions resulted in good decoder performance, though it appears that wS2 contains a richer functional diversity for orofacial movements that can be used to precisely reconstruct t-SNE trajectories. We used ethograms reconstructed from neuronal activity to decode the duration of lick bouts on a trial-by-trial basis (see STAR Methods). Accuracy in predicting lick bout duration was assessed by computing the Pearson correlation coefficient between observed and decoded lick bout durations across all trials of each session, with the highest correlation found in wS2 (Figure 4K). The rich representation of orofacial movements in wS2 could potentially originate from the large sensory integration known to take place in this associative area, while wM2 appears to be implicated in action initiation but less so in moment-by-moment execution. The latter is presumably taking place rather in primary motor areas such as

(E) Action tuning maps response along the reparametrized trajectories in the orofacial state space for each cortical area. This plot shows how the typical intensity of neuronal responses varies along the motor sequence of lick trials. Curves represent averages across all motor-related neurons of all sessions and mice in each population (wS1: $n = 115$, wS2: $n = 1195$, wM2: $n = 475$), shaded areas represent SEM. The color of the curves for each coordinate is given by a weighted average of colors representing the motor states traversed by the trajectory at that point across all sessions considered. Black dots: the distribution of preferred positions in the trajectory across sessions.

(F) Distributions of preferred positions displayed in (E) across populations. Vertical dashed lines represent maximum density peak positions. Inset: maximum density peak positions represented as bar plot along with error bars representing 95% confidence intervals obtained from a bootstrap procedure (see STAR Methods).

(G) Observed (left) and decoded (right) ethograms in Hit trials for an example wS1 imaging session (color legend for categories of motor states displayed below). Trials are ordered chronologically. Vertical white line represents C2 stimulus onset and the dashed white line represents the end of the response window.

(H) Same as (G) for an example wS2 imaging session.

(I) Same as (G) for an example wM2 imaging session.

(J) Distributions of motor state classification accuracy (fraction of correctly predicted states) across sessions. Violin plots represent full distributions of the average value of bin-by-bin decoding accuracy (see STAR Methods) for wS1 ($n = 24$), wS2 ($n = 42$), and wM2 ($n = 40$) recording sessions. Boxplots represent medians, interquartile range, and max/min without outliers (outside 1.5 times interquartile range from 1st and 4th quartile). * $p < 0.05$, * $p < 0.01$, and *** $p < 0.001$ (two-sided unpaired Wilcoxon test, wS1 vs. wS2: $p = 0.0078$; wS1 vs. wM2: $p = 0.033$; wM2 vs. wS2: $p = 0.0001$).

(K) Distributions of correlation between observed and decoded lick bout duration across sessions. Violin plots represent full distributions of Pearson correlation coefficients between observed and inferred lick bout durations for wS1 ($n = 24$), wS2 ($n = 42$), and wM2 ($n = 40$) recording sessions. Boxplots represent medians, interquartile range, and max/min without outliers (outside 1.5 times interquartile range from 1st and 4th quartile). * $p < 0.05$, ** $p < 0.01$, and *** $p < 0.001$ (two-sided unpaired Wilcoxon test, wS1 vs. wS2: $p = 3.2 \times 10^{-5}$; wS1 vs. wM2: $p = 0.027$; wM2 vs. wS2: $p = 5.5 \times 10^{-6}$).

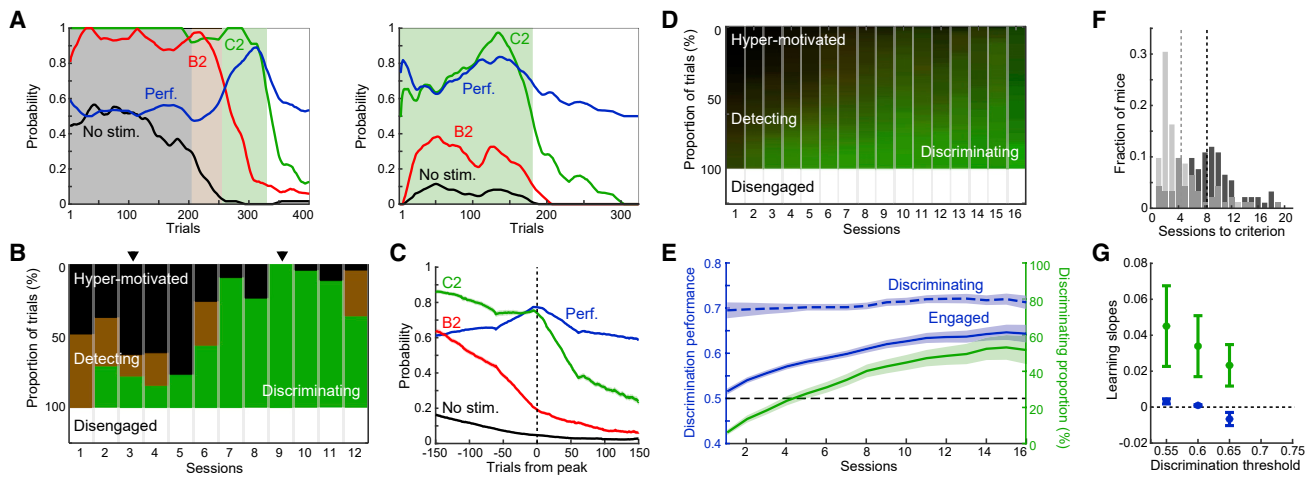


Figure 5. Mice exhibit distinct behavioral states within single sessions, reflecting changes in motivational level

(A) Probability of licking for all stimulus conditions and discrimination performance (blue) across trials for two sessions indicated with arrows in (B). Colored shaded patches highlight distinct behavioral states (gray: hyper-motivated, brown: detection, green: discrimination, white: disengaged, see STAR Methods and Figure S5).

(B) Proportion of trials spent on each behavioral state across sessions for an example mouse.

(C) Lick probability for all stimulus conditions and performance averaged across all mice ($N = 92$ mice) after centering each session on the trial displaying peak performance. Same color code as in (A). Shaded areas: SEM.

(D) Same as (B) but averaged over all mice ($N = 92$ mice) with graded colors corresponding in different mixture of behavioral states across mice for each session.

(E) Discrimination performance across sessions averaged across all mice ($N = 92$ mice) for all trials where mice were engaged (blue line) or for trials in the discriminating state only (dashed blue line). Dashed black line: chance level. The average proportion of trials spent in the discriminating state is shown in green with axis. Shaded areas: SEM.

(F) Histogram showing distributions of task performance rise times (number of training sessions required to reach 75% of peak performance) across all mice ($N = 92$) based on all engaged trials (dark gray) or only in trials in the discriminating state (light gray). Dashed lines represent averages for each distribution. Average task performance risetimes across all mice: 8.29 ± 0.43 sessions (engaged) versus 4.40 ± 0.37 sessions (discriminating) with significant difference: two-sided paired t test, $p = 1 \times 10^{-15}$.

(G) Estimated slopes for learning curves in discriminating state (blue) and proportion of trials in discriminating phase (green) in (E, threshold = 0.6) and for two other discrimination thresholds (0.55 and 0.65). Slopes were estimated around session 6 and error bars are 95% confidence intervals. See also Figure S5.

the tongue-jaw primary motor cortex (tjM1), as previously described (Mayrhofer et al., 2019; Xu et al., 2022).

Mice exhibit distinct behavioral states within single sessions, reflecting changes in motivational level

The linear decrease of lick bout duration with session progression (Figure 1F) reflects changes of thirst-related motivational level. Observing such non-stationarity in the level of motivation led us to more carefully inspect individual sessions to identify specific behavioral states related to changes in thirst. Across mice and sessions, we observed a stereotypical pattern of changes in the licking probabilities for different stimulus conditions. Using simple criteria on lick rates, we identified four behavioral states that we named “hyper-motivated,” “detecting,” “discriminating,” and “disengaged” (see STAR Methods and Figure S5). The hyper-motivated state was characterized by high spontaneous and evoked licking probability, detecting state was characterized by low spontaneous licking but poor discrimination, discriminating state was characterized by higher whisker discrimination, and disengaged state was characterized by low evoked licking (Figure 5A). These four distinct behavioral states reflect a discretization of continuous changes in motivational state over time based on qualitatively distinct task performances emerging throughout the course of every session.

As mice improved their average task performance, the relative proportion of these behavioral states changed from day to day (Figure 5B). Although the discriminating phase was short during the early days of training, mice could already reach high performance levels similar to those reached in the last days of training (Figure 5A). Discrimination performance during individual sessions displayed an “inverted U-shaped” curve with lower performance at the beginning and end of the session (Figure 5C). Across all mice we confirmed that the proportion of trials spent in the discriminating state increased during the training procedure (Figures 5D and 5E).

Most of the learning time course was dominated by changes in motivational control. Indeed, we found that the average discrimination performance during the discriminating state was already high during the first days of training, while the proportion of this state increased steadily over days (Figure 5E). The resemblance of the time course for overall performance during engaged states and the relative proportion of the discriminating phase indicated that most of the learning dynamics were driven by a control of behavioral state rather than sensorimotor association that is most likely acquired early during the training. This was supported by estimating the number of sessions necessary for each mouse to reach a stable performance (75% of overall peak performance) in the engaged state (all states except disengaged)

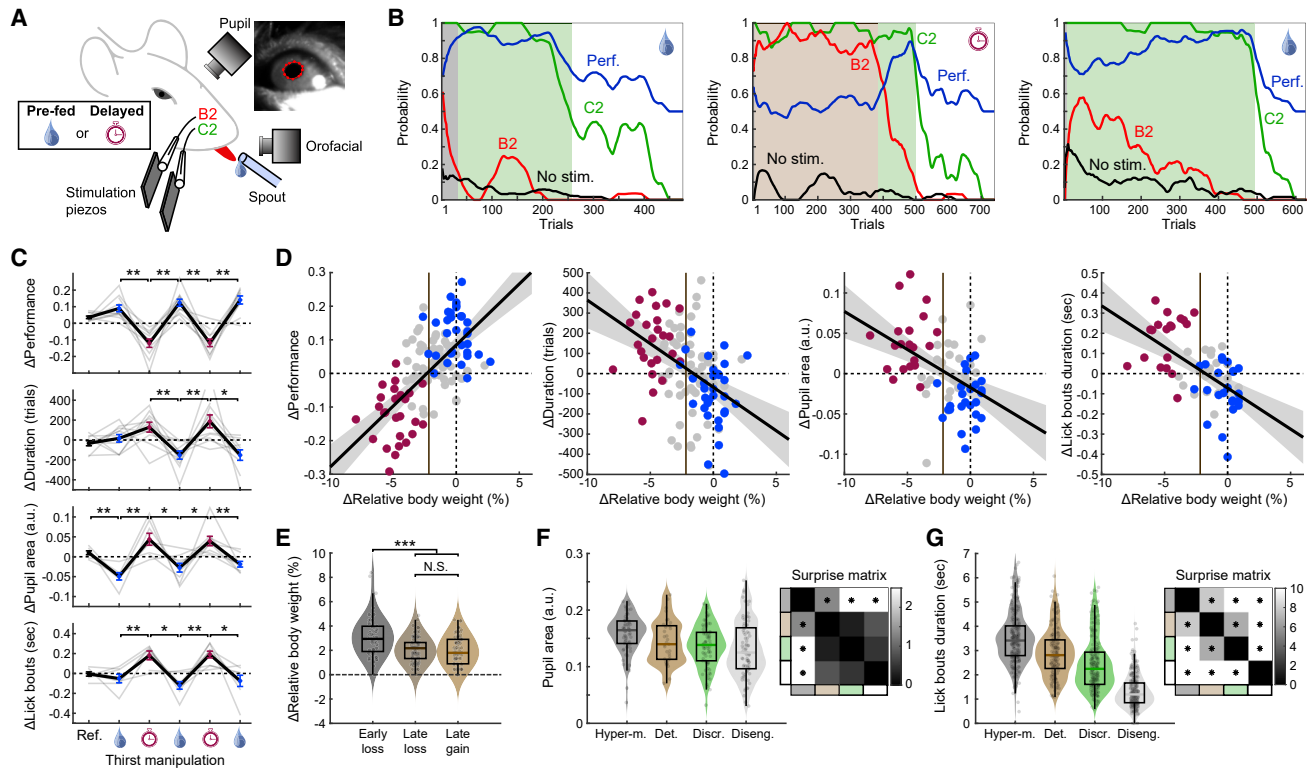


Figure 6. Thirst manipulation reversibly affects task performance, pupil dynamics, and licking behavior for water reward

(A) Schematic of the experimental design. Mice were subjected to cycles of thirst manipulation either by receiving water prior to the training (pre-fed) or by delaying the training (delayed). Orofacial movements and pupil dilation were filmed. Inset: example image of eye-filming field of view with estimated pupil contour markers shown in red.

(B) Example of 3 consecutive sessions where a mouse was first pre-fed (left), trained with delay (middle), and pre-fed again (right). Color code identical to Figure 5A.

(C) Changes in discrimination performance ($N = 11$ mice), session duration ($N = 11$ mice), pupil area ($N = 9$ mice), and lick bout duration ($N = 9$ mice) for consecutive days of thirst manipulation with pre-feeding (water drop) and delayed training (timer). Gray lines indicate individual mice and black lines indicate population average with error bars as SEM (two-sided paired Wilcoxon test, $*p < 0.05$ and $**p < 0.01$).

(D) Changes in discrimination performance ($n = 82$ sessions), session duration ($n = 82$ sessions), pupil area ($n = 57$ sessions), and lick bout duration ($n = 55$ sessions) as a function of weight difference between the end of a session and the beginning of the next one expressed in relative weight. Blue dots: pre-feeding sessions, red dots: delayed sessions, gray dots: sessions without thirst manipulation. Black lines indicate best linear fit with shaded areas as 95% confidence interval. Pearson correlation coefficients: performance (0.61 , $p = 8.6 \times 10^{-13}$), duration (-0.41 , $p = 4.1 \times 10^{-6}$), pupil area (-0.42 , $p = 0.00031$), and lick bouts duration (-0.57 , $p = 9.5 \times 10^{-7}$). p values are obtained from a t -distribution with 2 degrees of freedom. Vertical brown line indicates median weight loss of trained mice between two consecutive sessions.

(E) Distributions of weight loss (in relative values) for early ($n = 60$) and late ($n = 111$) sessions. The right violin plot shows the distribution of weight gained during task in late sessions ($n = 82$). $***p < 0.001$, N.S., not significant (two-sided unpaired Wilcoxon test, Early loss vs. Late loss: $p = 1.6 \times 10^{-6}$; Early loss vs. Late gain: $p = 7.5 \times 10^{-6}$; Late loss vs. Late gain: $p = 0.62$).

(F) Pupil area as a function of behavioral states ($n = 103$ sessions). One-way ANOVA $p = 0.0011$. Surprise matrix is shown on the right comparing all states (color coded on the side). Two-sided unpaired Wilcoxon test, $*p < 0.05$.

(G) Lick bout duration as a function of behavioral states ($n = 495$ sessions). One-way ANOVA $p = 3.1 \times 10^{-117}$. Surprise matrix is shown on the right comparing all states (color coded on the side). Two-sided unpaired Wilcoxon test, $*p < 0.05$.

(E–G) Boxplots represent medians, interquartile range, and max/min without outliers (outside 1.5 times interquartile range from 1st and 4th quartile).

compared to discriminating states only (Figure 5F). Mice showed much faster learning when computed for discriminating states compared to engaged states (4.40 ± 0.37 sessions for discriminating versus 8.29 ± 0.43 sessions for engaged with significant difference, two-sided paired t test, $p = 1 \times 10^{-15}$). Furthermore, this analysis was robust to the choice of threshold for classifying discriminating states. For different thresholds, we observed that the slopes describing changes of discriminating state proportions over days were larger than the slopes describing variation

of performance within that state over days (Figure 5G). The latter slopes were found to be close to 0. This analysis decouples two aspects of the learning process: the strength of the sensorimotor association, defined as the performance in the discriminating state, and the control of motivational state, defined as the proportion of the session spent in that state. Learning trajectories based on changes exclusively in one of these variables were numerically simulated and compared to mouse behavior (Figure S5, see STAR Methods). Although both learning trajectories

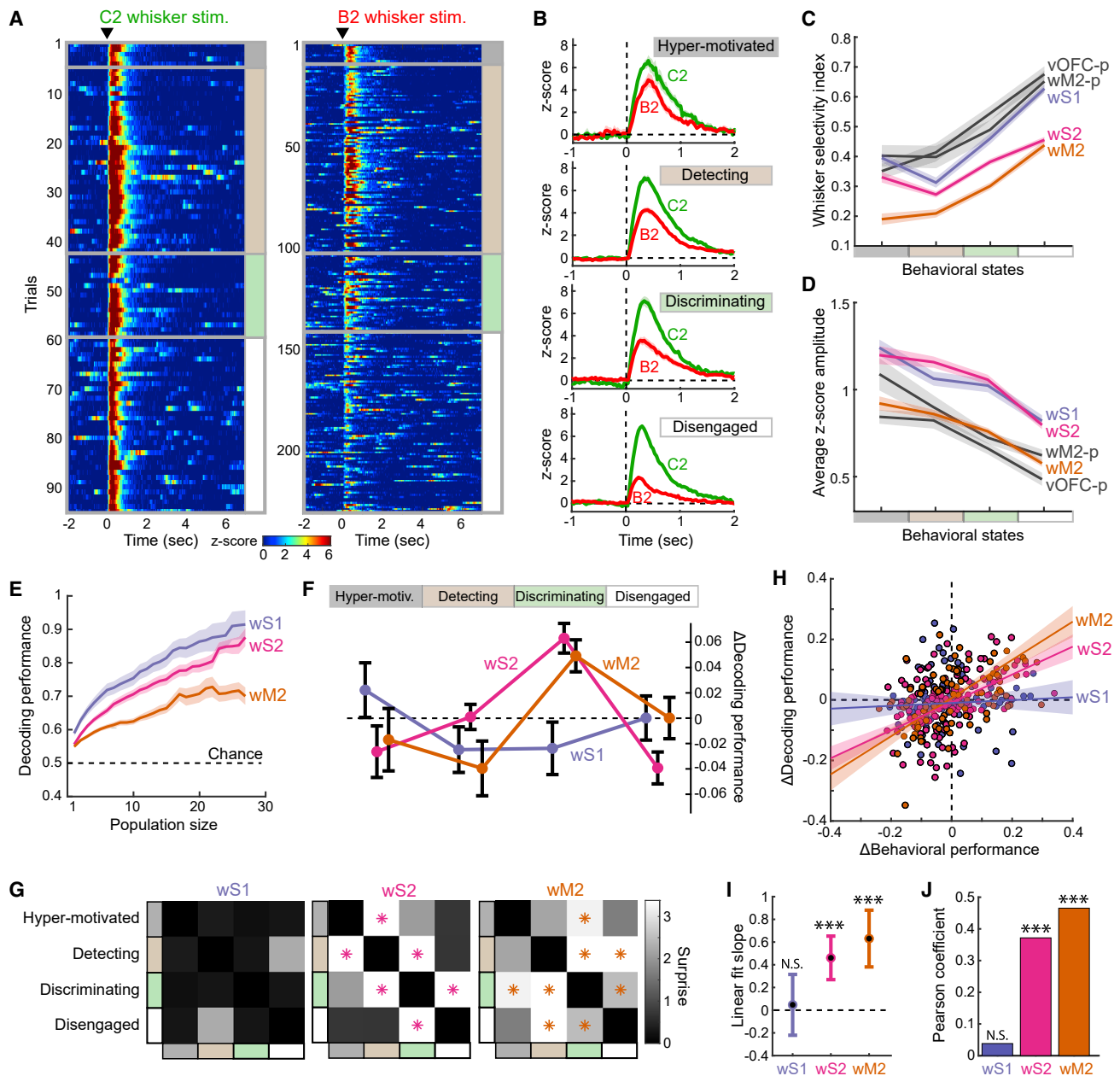


Figure 7. Whisker decoding in the secondary sensorimotor pathway correlates with task performance in different behavioral states

(A) Z scored calcium responses to C2 and B2 whisker stimulation across a session for an example neuron. Behavioral states are indicated in the right with color bars (gray: hyper-motivated, brown: detecting, green: discriminating, white: disengaged). Trials are ordered chronologically.

(B) Average response across trials in each behavioral state as indicated in (A). Shaded areas: SEM.

(C) Whisker Selectivity Index (WSI) for each neural population across behavioral states. Shaded areas: SEM.

(D) Average Z scored response amplitude across C2 and B2 whisker stimulation for each neural population across behavioral states. Shaded areas: SEM.

(E) Whisker decoding performance averaged over imaging sessions in wS1, wS2, and wM2 as a function of population size. Dashed black line: chance level. Shaded areas: SEM.

(F) Variation of decoding performance in each behavioral state for wS1, wS2, and wM2 populations. Points represent performance variation expressed as a relative difference from average performance across all states. One-way ANOVA wS1: $p = 0.36$; wS2: $p = 2.0 \times 10^{-6}$; wM2: $p = 0.0031$; Error bars: SEM.

(G) Surprise matrices for mean performance variation difference across all states. For each comparison, only sessions featuring the relevant pairs of states are kept (see STAR Methods). Color bars on the side indicate behavioral states. Surprise values plotted derive from p values obtained with a two-sided paired t test. * $p < 0.05$ with Bonferroni correction.

(H) Variation of decoding performance as a function of the variation of behavioral performance (both as relative difference from the average session value) for wS1 ($n = 86$), wS2 ($n = 143$), and wM2 ($n = 93$). Lines represent best linear fits. Shaded areas: 95% confidence region given uncertainty on best fit parameter values.

(legend continued on next page)

were indistinguishable in their average performance curves (Figures S5D and S5J), they displayed very different characteristics, supporting the hypothesis that mice in the two-whisker task increase their discrimination performance mainly through better control of motivational state.

Thirst manipulation reversibly affects task performance, pupil dynamics, and licking behavior for water reward

To directly test the effect of thirst-related motivation on task performance during training, we manipulated the level of thirst bidirectionally in consecutive training days (see STAR Methods). To reduce the level of thirst prior to training, we pre-fed mice with water an hour before the session began, whereas we increased the level of thirst by delaying the training session with respect to the normal schedule (Figure 6A). Orofacial movements and pupils were filmed during individual sessions to monitor licking behavior and pupil dilation as proxies for thirst-related motivation and arousal, respectively. Changes in thirst level had a dramatic effect on task performance. In consecutive sessions where mice were first pre-fed then trained with a delay, we observed a strong regression in task performance following the delay (Figure 6B). Although the average performance was much worse for the delayed session due to a decrease in the discriminating phase, the performance in that phase remained stable (Figure 6B, middle panel). This deterioration of average task performance could be completely reversed the following day by pre-feeding the mouse with water prior to training (Figure 6B, right panel). This was confirmed at the population level, where we found that consecutive days with pre-feeding or delayed training resulted in strong and reversible changes of task performance in a range comparable to normal learning (Figure 6C). Session duration was inversely affected with shorter sessions in days where mice were pre-fed and longer sessions in days with delayed training. Both pupil dilation and lick bout duration were also significantly affected by the manipulation of thirst level. Mice displayed more dilated pupils and produced longer bouts of licking in days with higher level of thirst and the converse in days with pre-feeding (Figure 6C).

To obtain a more graded relation of thirst level with these variables, we compared body weight changes from the end of a session to the beginning of the next. Body weights were computed relative to the weight prior to water restriction (see STAR Methods). We observed strong correlations between body weight changes and changes in task performance, session duration, pupil dilation, and lick bout duration (Figure 6D). Large body weight losses resulted in deterioration of task performance, longer sessions, more dilated pupils, and longer lick bout duration. For moderate body weight losses (<2%), we observed an increase in task performance and decrease in session duration, pupil dilation, and lick bout duration. Manipulations of thirst level allowed us to explore a large range of body weight loss/gain, revealing a linear relationship with critical behavioral variables. We posit that during learning of the task in water-restriction con-

ditions, mice learn to regulate their weight loss and therefore their thirst-related motivation. Indeed, we observed that mice lost significantly more weight during early days of training, as opposed to later days (Figure 6E). Interestingly, at expert level during late days of training, weight loss was comparable to weight gain during training, indicating that mice adapt to water-restriction conditions to maintain stable body weight and task performance across days (Figures 6D and 6E). This could be achieved by reduced motor activity and grooming in their home cage, as previously reported (Goltstein et al., 2018), or by physiological adaptations that occur in rodents after days of water scarcity (Xu and Wang, 2016).

Although both pupil dilation and lick bout duration were affected by manipulation of thirst level, they displayed different dependencies on behavioral states within sessions. Pupils were significantly more dilated during hyper-motivated states but comparable in other states (Figure 6F). Although we selected epochs without whisker stimuli or reward delivery to measure pupil dilation (quiet window, see STAR Methods), this proxy for arousal was noisy and therefore did not reflect variations in behavioral states. On the contrary, lick bout duration showed strong variations across behavioral states, decreasing almost linearly from the hyper-motivated to the disengaged state (Figure 6G). This indicates that lick bout duration for reward during task execution could be used as a reliable indicator of thirst-related motivation varying within and between training sessions.

Whisker decoding in the secondary sensorimotor pathway correlates with task performance across behavioral states

To test the impact of changes in motivational states on sensory representations, we focused on all sensory neurons that were not responding to isolated lick events (i.e., excluding mixed neurons to avoid contamination by motor-related signals). Single neuron examples showed that sensory neurons changed their whisker selectivity during single sessions as the mouse exhibited different behavioral states (Figure 7A). Responses to the preferred whisker were relatively constant across the session but, as motivation decreased, the response to the non-preferred whisker decreased (Figure 7B) in line with the stronger PMI value observed for the non-preferred whisker (Figure 3I). As a result, the whisker selectivity increased from the hyper-motivated to the disengaged state for all populations (Figure 7C). The overall whisker-evoked activity, however, was reduced with decreasing motivation (Figure 7D). While the whisker representation in these neuronal populations gained in resolution with decreasing motivation, it also lost in signal-to-noise ratio with respect to baseline activity.

To understand how these opposite effects can potentially alter perception, we used a Bayesian decoder to predict whisker identity from neuronal activity (see STAR Methods). The decoder performance was higher for neuronal populations with high whisker selectivity (Figure 3G) for all decoding pool sizes (Figure 7E). To understand whether perceptual capacity could be

(I) Slope parameters for best linear fits in (H). Confidence intervals and p values for difference from zero are obtained from the fit covariance matrix (see STAR Methods). Error bars indicate 95% confidence intervals. N.S., not significant (wS1: $p = 0.37$). *** $p < 0.001$ (wS2: $p = 1.2 \times 10^{-6}$; wM2: $p = 3.7 \times 10^{-7}$).

(J) Pearson correlation coefficients for the data shown in (H). p values are obtained from a t-distribution with 2 degrees of freedom. N.S., not significant (wS1: $p = 0.73$). *** $p < 0.001$ (wS2: $p = 4.9 \times 10^{-6}$; wM2: $p = 2.6 \times 10^{-6}$). See also Figure S6.

affected by the motivational state, we then compared the decoder performance of wS1, wS2, and wM2 populations in behavioral states described in Figure 5 (see STAR Methods). We observed that the secondary whisker sensorimotor pathway wS2-wM2, but not wS1, displayed a marked improvement in whisker prediction performance during the discriminating state in which mice performed the task best (Figure 7F). In other words, the inverted U-shaped pattern seen in whisker discrimination performance was also found in neuronal-activity-based whisker decoding performance as a “sweet spot” between increasing whisker selectivity and reduced response amplitude. When analyzed separately, gated and pure sensory neurons displayed similar changes across states, although decoding performance decreased more strongly for gated neurons in the disengaged state (Figure S6). The significance of this effect was confirmed by comparing exclusively neurons that were imaged during pairs of states (Figure 7G).

This result indicates that whisker-identity decoding performance from neuronal activity could potentially explain whisker discrimination performance in the perceptual decision-making task. For each session and motivational state, we compared the change in behavioral and decoder whisker discrimination performance with respect to the average values obtained for the whole session. We observed a strong correlation for wS2 and wM2, but not for wS1 (Figures 7H–7J), suggesting that whisker sensory representation in the secondary sensorimotor pathway covaries with the mouse’s performance. Hyper-motivated or disengaged states diminished sensory tuning or neuronal signal, respectively, which resulted in poorer decoding performance. When mice are in the discriminating phase, neuronal populations considerably improve their decoding capacity. Note that decoding from a full cortical population can overestimate the capacity of the brain to use sensory information in downstream areas involved in decision-making (Stringer et al., 2021). Indeed, only a fraction of neurons in wS2 will project their axons to convey a whisker sensory signal to wM2. As most of these projecting neurons are gated sensory neurons that display stronger modulations with behavioral state (Figure S6) and moderate whisker selectivity (Figure 3G), an increase or decrease of decoding performance in these populations can potentially have a strong impact on decision-making.

DISCUSSION

How behavioral states influence sensory processing is a central question in systems neuroscience. Exploratory behaviors, task engagement, and arousal have been shown to strongly influence sensory processing (Ayaz et al., 2013; Crochet and Petersen, 2006; Ferezou et al., 2007; Lee et al., 2020; McGinley et al., 2015; Szwed et al., 2003). Several studies have demonstrated how internal states related to thirst and hunger can reshape neural representations brain-wide (Allen et al., 2019; Burgess et al., 2016; Livneh et al., 2017). The impact of motivational or arousal states on decision-making has been extensively studied in psychology, dating back to the Yerkes-Dodson law introduced in the early 20th century (Yerkes and Dodson, 1908). This empirical law describes how performance of behavioral tasks increases with increasing task-pressure up

to a point where high pressure becomes detrimental and results in poorer performance. A recent study reported that very high or low arousal states measured by pupil dilation correlated with impaired performance in mice executing a detection task (McGinley et al., 2015), in line with the Yerkes-Dodson law. Here, we showed that water-restricted mice exhibit distinct behavioral states in a two-whisker discrimination task. As thirst-induced motivational pressure decreased, performance varied following an “inverted-U shaped” curve reminiscent of the Yerkes-Dodson law, with the best performance occurring in a state of intermediate motivational pressure. We investigated the neural basis of this phenomenon and observed degraded sensory representations at the extremes of the spectrum of motivational pressure. Our work sheds new light on the perceptual side of a pervasive phenomenon shaping human and animal goal-directed behaviors.

Where do the signals modifying the whisker representations originate from? Hypothalamic neurons sensing osmolarity and angiotensin participate in a circuit capable of integrating different physiological signals (Stemson, 2013) to compute internal states such as “thirst” and subsequently broadcast them to the rest of the brain (Allen et al., 2019). The exact mechanism through which state-defining signals are broadcasted and how they affect sensorimotor transformation is not yet fully elucidated. Both fast synaptic transmission and/or neuromodulators are likely involved. Noradrenergic (NA) projections from locus coeruleus and cholinergic (ACh) projections from basal forebrain are known to regulate brain states during arousal, vigilance, and attention (Harris and Thiele, 2011; Lee and Dan, 2012). Cholinergic inputs have been reported to affect response properties of sensory neurons (Chen et al., 2015; Fu et al., 2014; Gasselino et al., 2021; Goard et al., 2016; Pinto et al., 2013). Noradrenergic neurotransmission is also related with arousal and has been shown to modulate neuronal firing in mouse sensory cortices (Polack et al., 2013) together with pupil dilation (Breton-Provencher and Sur, 2019). It is possible that abnormally high levels of neuromodulator release could lead to broadening of tuning properties in sensory cortices, such as observed in hyper-motivated states. This widespread increase in sensory-evoked activity could improve simple detection while being detrimental for discrimination. The existence of an adaptive, nutritional-state-dependent trade-off between sensory coding precision and metabolic expenditure has been reported in mice (Padamsey et al., 2021). It is possible that the effect we observed could have a similar adaptive nature on a shorter timescale.

Our behavioral findings have profound implications about the nature of the learning process in goal-directed sensorimotor tasks in water-restricted mice. Different aspects of behavioral task procedures, such as the availability of a positive reinforcer or lack of habituation to experimental conditions, can mask an already acquired latent knowledge. This highlights the importance of decoupling knowledge acquisition and expression in interpreting the results of behavioral experiments (Kuchibhotla et al., 2019). We report here two separate processes going on throughout the training: a fast increase of sensorimotor association during discriminating states and a slower improvement of the ability to remain in that state. Drawing a clear distinction between these two processes could be key to properly interpreting

future experiments aiming at tracking network plasticity at the synaptic level underlying acquisition of task associations (Humeau and Choquet, 2019).

Characterization of sensory and motor-related responses along the wS1-wS2-wM2 pathway revealed a functional specialization of these areas. Gated sensory neurons responded selectively to sensorimotor events, therefore displaying a form of context-dependent coding of sensory stimuli preceding intentional action. Increase in the number of gated sensory neurons across the wS1-wS2-wM2 pathway complements other recent reports suggesting that this pathway is required for tactile-based sensorimotor transformation in rodents (Crochet et al., 2019; Esmaeili et al., 2020, 2021) and monkeys (Romo and Rossi-Pool, 2020). Gated sensory neurons respond to whisker stimuli only when mice intend to lick. These cells are characterized by a high pre-lick modulation index, displaying an extreme version of the decision-related modulations reported in previous studies (Kwon et al., 2016; Yamashita and Petersen, 2016; Yang et al., 2016). The enrichment of this type of neuron among projection neurons from wS2 to its two main frontal targets, wM2 and vOFC, could gate the routing of sensory information toward regions involved in action planning and execution.

STAR★METHODS

Detailed methods are provided in the online version of this paper and include the following:

- **KEY RESOURCES TABLE**
- **RESOURCE AVAILABILITY**
 - Lead contact
 - Materials availability
 - Data and code availability
- **EXPERIMENTAL MODEL AND SUBJECT DETAILS**
- **METHOD DETAILS**
 - Head plate surgery
 - Cranial window surgery for two-photon imaging
 - Behavioral training
 - High-speed filming and analysis of orofacial movements
 - High-speed filming and analysis of pupil dilation
 - Wide-field imaging
 - Perfusion and postmortem analysis
 - Optogenetics
 - Two-photon imaging
 - Two-photon calcium data pre-processing
 - Behavioral analysis and state classification
 - Simulations of learning trajectories
 - Classification of neurons in functional cell classes
 - Quantification of whisker selectivity
 - Quantification of pre-lick modulation in sensory responses
 - Clustering of populations according to similarities in pre-lick modulation
 - Analysis of action tuning maps
 - Decoding the identity of the stimulated whisker
 - Decoding orofacial movements
 - Quantification and statistical analysis

SUPPLEMENTAL INFORMATION

Supplemental information can be found online at <https://doi.org/10.1016/j.neuron.2022.09.032>.

ACKNOWLEDGMENTS

We thank members of the El-Boustani and the Petersen laboratories for discussions. This work was supported by the Swiss National Science Foundation: PCEFP3_181070 (S.E.-B.), CRSII5_177237 (C.C.H.P.), and 31003A_182010 (C.C.H.P.).

AUTHOR CONTRIBUTIONS

G.M., M.G., J.M.M., M.A., G.F., C.C.H.P., and S.E.-B. participated in conception and design of research. G.M., M.G., J.M.M., M.A., and S.E.-B. performed experiments, analyzed data and prepared figures. G.M., C.C.H.P., and S.E.-B. wrote the manuscript.

DECLARATION OF INTERESTS

C.C.H.P. is a member of the advisory board of *Neuron*.

INCLUSION AND DIVERSITY

We support inclusive, diverse, and equitable conduct of research.

Received: March 13, 2022

Revised: July 25, 2022

Accepted: September 24, 2022

Published: October 13, 2022

REFERENCES

- Allen, W.E., Chen, M.Z., Pichamoorthy, N., Tien, R.H., Pachitariu, M., Luo, L., and Deisseroth, K. (2019). Thirst regulates motivated behavior through modulation of brainwide neural population dynamics. *Science* 364 (6437). <https://doi.org/10.1126/science.aav3932>.
- Allen, W.E., Kauvar, I.v., Chen, M.Z., Richman, E.B., Yang, S.J., Chan, K., Gradinaru, V., Deverman, B.E., Luo, L., and Deisseroth, K. (2017). Global representations of goal-directed behavior in distinct cell types of mouse neocortex. *Neuron* 94, 891–907.e6. <https://doi.org/10.1016/j.neuron.2017.04.017>.
- Ayaz, A., Saleem, A.B., Schölvinck, M.L., and Carandini, M. (2013). Locomotion controls spatial integration in mouse visual cortex. *Curr. Biol.* 23, 890–894. <https://doi.org/10.1016/j.cub.2013.04.012>.
- Barthas, F., and Kwan, A.C. (2017). Secondary motor cortex: where 'sensory' meets 'motor' in the rodent frontal cortex. *Trends Neurosci.* 40, 181–193. <https://doi.org/10.1016/j.tins.2016.11.006>.
- Berman, G.J., Choi, D.M., Bialek, W., and Shaevitz, J.W. (2014). Mapping the stereotyped behaviour of freely moving fruit flies. *J. R. Soc. Interface* 11, 20140672. <https://doi.org/10.1098/rsif.2014.0672>.
- Berndt, A., Lee, S.Y., Wietek, J., Ramakrishnan, C., Steinberg, E.E., Rashid, A.J., Kim, H., Park, S., Santoro, A., Frankland, P.W., et al. (2016). Structural foundations of optogenetics: determinants of channelrhodopsin ion selectivity. *Proc. Natl. Acad. Sci. USA* 113, 822–829. <https://doi.org/10.1073/pnas.1523341113>.
- Breton-Provencher, V., and Sur, M. (2019). Active control of arousal by a locus coeruleus GABAergic circuit. *Nat. Neurosci.* 22, 218–228. <https://doi.org/10.1038/s41593-018-0305-z>.
- Burgess, C.R., Ramesh, R.N., Sugden, A.U., Levandowski, K.M., Minnig, M.A., Fenselau, H., Lowell, B.B., and Andermann, M.L. (2016). Hunger-dependent enhancement of food cue responses in mouse postrhinal cortex and lateral amygdala. *Neuron* 91, 1154–1169. <https://doi.org/10.1016/j.neuron.2016.07.032>.

- Chen, J.L., Carta, S., Soldado-Magraner, J., Schneider, B.L., and Helmchen, F. (2013a). Behaviour-dependent recruitment of long-range projection neurons in somatosensory cortex. *Nature* 499, 336–340. <https://doi.org/10.1038/nature12236>.
- Chen, N., Sugihara, H., and Sur, M. (2015). An acetylcholine-activated microcircuit drives temporal dynamics of cortical activity. *Nat. Neurosci.* 18, 892–902. <https://doi.org/10.1038/nn.4002>.
- Chen, T.-W., Wardill, T.J., Sun, Y., Pulver, S.R., Renninger, S.L., Baohan, A., Schreiter, E.R., Kerr, R.A., Orger, M.B., Jayaraman, V., et al. (2013b). Ultrasensitive fluorescent proteins for imaging neuronal activity. *Nature* 499, 295–300. <https://doi.org/10.1038/nature12354>.
- Crochet, S., and Petersen, C.C.H. (2006). Correlating whisker behavior with membrane potential in barrel cortex of awake mice. *Nat. Neurosci.* 9, 608–610. <https://doi.org/10.1038/nn1690>.
- Crochet, S., Lee, S.H., and Petersen, C.C.H. (2019). Neural circuits for goal-directed sensorimotor transformations. *Trends Neurosci.* 42, 66–77. <https://doi.org/10.1016/j.tins.2018.08.011>.
- Daigle, T.L., Madisen, L., Hage, T.A., Valley, M.T., Knoblich, U., Larsen, R.S., Takeno, M.M., Huang, L., Gu, H., Larsen, R., et al. (2018). A Suite of Transgenic Driver and Reporter Mouse Lines with Enhanced Brain-Cell-Type Targeting and Functionality. *Cell* 174, 465–480.e22. <https://doi.org/10.1016/j.cell.2018.06.035>.
- Dana, H., Mohar, B., Sun, Y., Narayan, S., Gordus, A., Hasseman, J.P., Tsegaye, G., Holt, G.T., Hu, A., Walpita, D., et al. (2016). Sensitive red protein calcium indicators for imaging neural activity. *elife* 5, 127277–e12824. <https://doi.org/10.7554/eLife.12727>.
- Efron, B., and Tibshirani, R.J. (1993). *An introduction to the bootstrap* (Boston, MA: Springer US).
- El-Boustani, S., Sermet, B.S., Foustoukos, G., Oram, T.B., Yizhar, O., and Petersen, C.C.H. (2020). Anatomically and functionally distinct thalamocortical inputs to primary and secondary mouse whisker somatosensory cortices. *Nat. Commun.* 11, 3342–3412. <https://doi.org/10.1038/s41467-020-17087-7>.
- Esmaeili, V., Oryshchuk, A., Asri, R., Tamura, K., Foustoukos, G., Liu, Y., Guiet, R., Crochet, S., and Petersen, C.C.H. (2022). Learning-related congruent and incongruent changes of excitation and inhibition in distinct cortical areas. *PLoS Biol.* 20, e3001667. <https://doi.org/10.1371/journal.pbio.3001667>.
- Esmaeili, V., Tamura, K., Foustoukos, G., Oryshchuk, A., Crochet, S., and Petersen, C.C. (2020). Cortical circuits for transforming whisker sensation into goal-directed licking. *Curr. Opin. Neurobiol.* 65, 38–48. <https://doi.org/10.1016/j.conb.2020.08.003>.
- Esmaeili, V., Tamura, K., Muscinelli, S.P., Modirshanechi, A., Boscaglia, M., Lee, A.B., Oryshchuk, A., Foustoukos, G., Liu, Y., Crochet, S., et al. (2021). Rapid suppression and sustained activation of distinct cortical regions for a delayed sensory-triggered motor response. *Neuron* 109, 2183–2201.e9. <https://doi.org/10.1016/j.neuron.2021.05.005>.
- Fenko, L., Yizhar, O., and Deisseroth, K. (2011). The development and application of optogenetics. *Annu. Rev. Neurosci.* 34, 389–412. <https://doi.org/10.1146/ANNUREV-NEURO-061010-113817>.
- Ferezou, I., Haiss, F., Gentet, L.J., Aronoff, R., Weber, B., and Petersen, C.C.H. (2007). Spatiotemporal dynamics of cortical sensorimotor integration in behaving mice. *Neuron* 56, 907–923. <https://doi.org/10.1016/j.neuron.2007.10.007>.
- Fu, Y., Tucciarone, J.M., Espinosa, J.S., Sheng, N., Darcy, D.P., Nicoll, R.A., Huang, Z.J., and Stryker, M.P. (2014). A cortical circuit for gain control by behavioral state. *Cell* 156, 1139–1152. <https://doi.org/10.1016/j.cell.2014.01.050>.
- Gassel, C., Hohl, B., Vernet, A., Crochet, S., and Petersen, C.C.H. (2021). Cell-type-specific nicotinic input disinhibits mouse barrel cortex during active sensing. *Neuron* 109, 778–787.e3. <https://doi.org/10.1016/j.neuron.2020.12.018>.
- Gilad, A., Gallero-Salas, Y., Groos, D., and Helmchen, F. (2018). Behavioral strategy determines frontal or posterior location of short-term memory in neocortex. *Neuron* 99, 814–828.e7. <https://doi.org/10.1016/j.neuron.2018.07.029>.
- Giovannucci, A., Pnevmatikakis, E.A., Devereett, B., Pereira, T., Fondriest, J., Brady, M.J., Wang, S.S.-H., Abbas, W., Parés, P., and Masip, D. (2018). Automated gesture tracking in head-fixed mice. *J. Neurosci. Methods* 300, 184–195. <https://doi.org/10.1016/j.jneumeth.2017.07.014>.
- Goard, M.J., Pho, G.N., Woodson, J., and Sur, M. (2016). Distinct roles of visual, parietal, and frontal motor cortices in memory-guided sensorimotor decisions. *Elife* 5, 1137644–e13830. <https://doi.org/10.7554/eLife.13764>.
- Goltstein, P.M., Reinert, S., Bonhoeffer, T., and Hübener, M. (2021). Mouse visual cortex areas represent perceptual and semantic features of learned visual categories. *Nat. Neurosci.* 24, 1441–1451. <https://doi.org/10.1038/s41593-021-00914-5>.
- Goltstein, P.M., Reinert, S., Glas, A., Bonhoeffer, T., and Hübener, M. (2018). Food and water restriction lead to differential learning behaviors in a head-fixed two-choice visual discrimination task for mice. *PLoS One* 13, e0204066. <https://doi.org/10.1371/journal.pone.0204066>.
- Grant, R.A., and Goss, V.G.A. (2022). What can whiskers tell us about mammalian evolution, behaviour, and ecology? *Mamm. Rev.* 52, 148–163. <https://doi.org/10.1111/mam.12253>.
- Guo, Z., Li, N., Huber, D., Ophir, E., Gutnisky, D., Ting, J.T., Feng, G., and Svoboda, K. (2014). Flow of cortical activity underlying a tactile decision in mice. *Neuron* 81, 179–194. <https://doi.org/10.1016/j.neuron.2013.10.020>.
- Harrell, E.R., Renard, A., and Bathellier, B. (2021). Fast cortical dynamics encode tactile grating orientation during active touch. *Sci. Adv.* 7, eabf7096. <https://doi.org/10.1126/sciadv.abf7096>.
- Harris, K.D., and Thiele, A. (2011). Cortical state and attention. *Nat. Rev. Neurosci.* 12, 509–523. <https://doi.org/10.1038/nrn3084>.
- Henschke, J.U., Dylida, E., Katsanevaki, D., Dupuy, N., Currie, S.P., Amvrosiadis, T., Pakan, J.M.P., and Rochefort, N.L. (2020). Reward association enhances stimulus-specific representations in primary visual cortex. *Curr. Biol.* 30, 1866–1880.e5. <https://doi.org/10.1016/j.cub.2020.03.018>.
- Hnasko, T.S., Perez, F.A., Scouras, A.D., Stoll, E.A., Gale, S.D., Luquet, S., Phillips, P.E.M., Kremer, E.J., and Palmiter, R.D. (2006). Cre recombinase-mediated restoration of nigrostriatal dopamine in dopamine-deficient mice reverses hypophagia and bradykinesia. *Proc. Natl. Acad. Sci. USA.* 103, 8858–8863. <https://doi.org/10.1073/pnas.0603081103>.
- Humeau, Y., and Choquet, D. (2019). The next generation of approaches to investigate the link between synaptic plasticity and learning. *Nat. Neurosci.* 22, 1536–1543. <https://doi.org/10.1038/s41593-019-0480-6>.
- Jazayeri, M., and Movshon, J.A. (2006). Optimal representation of sensory information by neural populations. *Nat. Neurosci.* 9, 690–696. <https://doi.org/10.1038/nn1691>.
- Kim, T.H., and Schnitzer, M.J. (2022). Fluorescence imaging of large-scale neural ensemble dynamics. *Cell* 185, 9–41. <https://doi.org/10.1016/j.cell.2021.12.007>.
- Komiyama, T., Sato, T.R., O'Connor, D.H., Zhang, Y.-X., Huber, D., Hooks, B.M., Gabbito, M., and Svoboda, K. (2010). Learning-related fine-scale specificity imaged in motor cortex circuits of behaving mice. *Nature* 464, 1182–1186. <https://doi.org/10.1038/nature08897>.
- Kuchibhotla, K. v., Gill, J. v., Lindsay, G.W., Papadoyannis, E.S., Field, R.E., Sten, T.A.H., Miller, K.D., and Froemke, R.C. (2017). Parallel processing by cortical inhibition enables context-dependent behavior. *Nat. Neurosci.* 20, 62–71. <https://doi.org/10.1038/nn.4436>.
- Kuchibhotla, K.V., Hindmarsh Sten, T., Papadoyannis, E.S., Elnozahy, S., Fogelson, K.A., Kumar, R., Boubenec, Y., Holland, P.C., Ostojic, S., and Froemke, R.C. (2019). Dissociating task acquisition from expression during learning reveals latent knowledge. *Nat. Commun.* 10, 2151. <https://doi.org/10.1038/s41467-019-10089-0>.
- Kwon, S.E., Yang, H., Minamisawa, G., and O'Connor, D.H. (2016). Sensory and decision-related activity propagate in a cortical feedback loop during

- touch perception. *Nat. Neurosci.* 19, 1243–1249. <https://doi.org/10.1038/nn.4356>.
- Lee, C.C.Y., Kheradpezhoh, E., Diamond, M.E., and Arabzadeh, E. (2020). State-dependent changes in perception and coding in the mouse somatosensory cortex. *Cell Rep.* 32, 108197. <https://doi.org/10.1016/j.celrep.2020.108197>.
- Le Merre, P., Esmaili, V., Charrière, E., Galan, K., Salin, P.-A., Petersen, C.C.H., and Crochet, S. (2018). Reward-based learning drives rapid sensory signals in medial prefrontal cortex and dorsal hippocampus necessary for goal-directed behavior. *Neuron* 97, 83–91.e5. <https://doi.org/10.1016/j.neuron.2017.11.031>.
- Lee, S.-H., and Dan, Y. (2012). Neuromodulation of brain states. *Neuron* 76, 209–222. <https://doi.org/10.1016/j.neuron.2012.09.012>.
- Livneh, Y., Ramesh, R.N., Burgess, C.R., Levandowski, K.M., Madara, J.C., Fenselau, H., Goldey, G.J., Diaz, V.E., Jikomes, N., Resch, J.M., et al. (2017). Homeostatic circuits selectively gate food cue responses in insular cortex. *Nature* 546, 611–616. <https://doi.org/10.1038/nature22375>.
- Livneh, Y., Sugden, A.U., Madara, J.C., Essner, R.A., Flores, V.I., Sugden, L.A., Resch, J.M., Lowell, B.B., and Andermann, M.L. (2020). Estimation of current and future physiological states in insular cortex. *Neuron* 105, 1094–1111.e10. <https://doi.org/10.1016/j.neuron.2019.12.027>.
- Ma, W.J., Beck, J.M., Latham, P.E., and Pouget, A. (2006). Bayesian inference with probabilistic population codes. *Nat. Neurosci.* 9, 1432–1438. <https://doi.org/10.1038/nn1790>.
- Mathis, A., Mamidanna, P., Cury, K.M., Abe, T., Murthy, V.N., Weyand Mathis, M., and Bethge, M. (2018). DeepLabCut: markerless pose estimation of user-defined body parts with deep learning. *Nat. Neurosci.* 21, 1281–1289. <https://doi.org/10.1038/s41593-018-0209-y>.
- Mayrhofer, J.M., El-Boustani, S., Foustoukos, G., Auffret, M., Tamura, K., and Petersen, C.C.H. (2019). Distinct contributions of whisker sensory cortex and tongue-jaw motor cortex in a goal-directed sensorimotor transformation. *Neuron* 103, 1034–1043.e5. <https://doi.org/10.1016/j.neuron.2019.07.008>.
- McGinley, M.J., David, S. v, and McCormick, D.A. (2015). Cortical membrane potential signature of optimal states for sensory signal detection. *Neuron* 87, 179–192. <https://doi.org/10.1016/j.neuron.2015.05.038>.
- Musall, S., Kaufman, M.T., Juavinett, A.L., Gluf, S., and Churchland, A.K. (2019). Single-trial neural dynamics are dominated by richly varied movements. *Nat. Neurosci.* 22, 1677–1686. <https://doi.org/10.1038/s41593-019-0502-4>.
- Pachitariu, M., Stringer, C., Dipoppa, M., Schröder, S., Rossi, L.F., Dalgleish, H., Carandini, M., and Harris, K.D. (2016). Suite2p: beyond 10,000 neurons with standard two-photon microscopy. Preprint at bioRxiv, 061507. <https://doi.org/10.1101/061507>.
- Padamsey, Z., Katsanevaki, D., Dupuy, N., and Rochefort, N.L. (2021). Neocortex saves energy by reducing coding precision during food scarcity. *Neuron* 110, 280–296.e10. <https://doi.org/10.1016/j.neuron.2021.10.024>.
- Parker, A.J., and Newsome, W.T. (1998). Sense and the single neuron: Probing the physiology of perception. *Annu. Rev. Neurosci.* 21, 227–277. <https://doi.org/10.1146/ANNUREV.NEURO.21.1.227>.
- Paxinos, G., and Franklin, K.B.J. (2000). *The mouse brain in stereotaxic coordinates* (Academic Press Inc).
- Pereira, T.D., Tabris, N., Matsliah, A., Turner, D.M., Li, J., Ravindranath, S., Papadoyannis, E.S., Normand, E., Deutsch, D.S., Wang, Z.Y., et al. (2022). Publisher correction: SLEAP: A deep learning system for multi-animal pose tracking. *Nat. Methods* 19, 628. <https://doi.org/10.1038/s41592-022-01495-2>.
- Pinto, L., and Dan, Y. (2015). Cell-type-specific activity in prefrontal cortex during goal-directed behavior. *Neuron* 87, 437–450. <https://doi.org/10.1016/j.neuron.2015.06.021>.
- Pinto, L., Goard, M.J., Estandian, D., Xu, M., Kwan, A.C., Lee, S.-H., Harrison, T.C., Feng, G., and Dan, Y. (2013). Fast modulation of visual perception by basal forebrain cholinergic neurons. *Nat. Neurosci.* 16, 1857–1863. <https://doi.org/10.1038/nn.3552>.
- Polack, P.-O., Friedman, J., and Golshani, P. (2013). Cellular mechanisms of brain state-dependent gain modulation in visual cortex. *Nat. Neurosci.* 16, 1331–1339. <https://doi.org/10.1038/nn.3464>.
- Romo, R., and Rossi-Pool, R. (2020). Turning touch into perception. *Neuron* 105, 16–33. <https://doi.org/10.1016/j.neuron.2019.11.033>.
- Sachidhanandam, S., Sreenivasan, V., Kyriakatos, A., Kremer, Y., and Petersen, C.C.H. (2013). Membrane potential correlates of sensory perception in mouse barrel cortex. *Nat. Neurosci.* 16, 1671–1677. <https://doi.org/10.1038/nn.3532>.
- Schindelin, J., Arganda-Carreras, I., Frise, E., Kaynig, V., Longair, M., Pietzsch, T., Preibisch, S., Rueden, C., Saalfeld, S., Schmid, B., et al. (2012). Fiji: an open-source platform for biological-image analysis. *Nat. Methods* 9, 676–682. <https://doi.org/10.1038/nmeth.2019>.
- Steinmetz, N.A., Zatzka-Haas, P., Carandini, M., and Harris, K.D. (2019). Distributed coding of choice, action and engagement across the mouse brain. *Nature* 576, 266–273. <https://doi.org/10.1038/s41586-019-1787-x>.
- Sternson, S.M. (2013). Hypothalamic survival circuits: Blueprints for purposive behaviors. *Neuron* 77, 810–824. <https://doi.org/10.1016/j.neuron.2013.02.018>.
- Stringer, C., Michaelos, M., Tsyboulski, D., Lindo, S.E., and Pachitariu, M. (2021). High-precision coding in visual cortex. *Cell* 184, 2767–2778.e15. <https://doi.org/10.1016/j.cell.2021.03.042>.
- Stringer, C., Pachitariu, M., Steinmetz, N., Reddy, C.B., Carandini, M., and Harris, K.D. (2019). Spontaneous behaviors drive multidimensional, brainwide activity. *Science*, 255. 1979. <https://doi.org/10.1126/science.aav7893>.
- Sul, J.H., Jo, S., Lee, D., and Jung, M.W. (2011). Role of rodent secondary motor cortex in value-based action selection. *Nat. Neurosci.* 14, 1202–1208. <https://doi.org/10.1038/nn.2881>.
- Szwed, M., Bagdasarian, K., and Ahissar, E. (2003). Encoding of vibrissal active touch. *Neuron* 40, 621–630. [https://doi.org/10.1016/S0896-6273\(03\)00671-8](https://doi.org/10.1016/S0896-6273(03)00671-8).
- Takahashi, N., Oertner, T.G., Hegemann, P., and Larkum, M.E. (2016). Active cortical dendrites modulate perception. *Science* 354, 1587–1590. <https://doi.org/10.1126/science.aah6066>.
- Van Der Maaten, L.J.P., and Hinton, G.E. (2008). Visualizing high-dimensional data using t-SNE. *J. Mach. Learn. Res.* 9, 2579–2605.
- Vinck, M., Batista-Brito, R., Knoblich, U., and Cardin, J.A. (2015). Arousal and locomotion make distinct contributions to cortical activity patterns and visual encoding. *Neuron* 86, 740–754. <https://doi.org/10.1016/j.neuron.2015.03.028>.
- Xin, Y., Zhong, L., Zhang, Y., Zhou, T., Pan, J., and Xu, N.L. (2019). Sensory-to-category transformation via dynamic reorganization of ensemble structures in mouse auditory cortex. *Neuron* 103, 909–921.e6. <https://doi.org/10.1016/j.neuron.2019.06.004>.
- Xu, D., Dong, M., Chen, Y., Delgado, A.M., Hughes, N.C., Zhang, L., and O'Connor, D.H. (2022). Cortical processing of flexible and context-dependent sensorimotor sequences. *Nature* 603, 464–469. <https://doi.org/10.1038/s41586-022-04478-7>.
- Xu, M.-M., and Wang, D.-H. (2016). Water deprivation up-regulates urine osmolality and renal aquaporin 2 in Mongolian gerbils (*Meriones unguiculatus*). *Comp. Biochem. Physiol. Mol. Integr. Physiol.* 194, 37–44. <https://doi.org/10.1016/j.cbpa.2016.01.015>.
- Yamashita, T., and Petersen, C.C. (2016). Target-specific membrane potential dynamics of neocortical projection neurons during goal-directed behavior. *eLife* 5 (e15798). <https://doi.org/10.7554/eLife.15798>.
- Yamashita, T., Vavladeli, A., Pala, A., Galan, K., Crochet, S., Petersen, S.S.A., and Petersen, C.C.H. (2018). Diverse long-range axonal projections of excitatory layer 2/3 neurons in mouse barrel cortex. *Front. Neuroanat.* 12, 33. <https://doi.org/10.3389/fnana.2018.00033>.
- Yang, H., Kwon, S.E., Severson, K.S., and O'Connor, D.H. (2016). Origins of choice-related activity in mouse somatosensory cortex. *Nat. Neurosci.* 19, 127–134. <https://doi.org/10.1038/nn.4183>.

Yerkes, R.M., and Dodson, J.D. (1908). The relation of strength of stimulus to rapidity of habit-formation. *J. Comp. Neurol. Psychol.* *18*, 459–482. <https://doi.org/10.1002/cne.920180503>.

Zhang, S., Xu, M., Chang, W.-C., Ma, C., Hoang Do, J.P., Jeong, D., Lei, T., Fan, J.L., and Dan, Y. (2016). Organization of long-range inputs and outputs

of frontal cortex for top-down control. *Nat. Neurosci.* *19*, 1733–1742. <https://doi.org/10.1038/nn.4417>.

Zingg, B., Chou, X.L., Zhang, Z.G., Mesik, L., Liang, F., Tao, H.W., and Zhang, L.I. (2017). AAV-mediated anterograde transsynaptic tagging: mapping corticocollicular input-defined neural pathways for defense behaviors. *Neuron* *93*, 33–47. <https://doi.org/10.1016/j.neuron.2016.11.045>.

STAR★METHODS

KEY RESOURCES TABLE

REAGENT or RESOURCE	SOURCE	IDENTIFIER
Bacterial and virus strains		
Canine adenovirus expressing Cre recombinase (CAV2-Cre) retrogradely	Biocampus Montpellier - Hnasko et al., 2006	https://plateau-igmm.pvm.cnrs.fr/?vector=cav-cre
AAV1.hSyn.eGFP.WPRE.bGH	UPenn Vector Core	AV-1-PV1696
AAV1.Syn.Flex.NES-jRGECO1a.WRPE.SV40	UPenn Vector Core	CS0873
AAV1.CamKII0.4.Cre.SV40	UPenn Vector Core	CS0843
ssAAV-hSyn1-chI-EBFP2_2A-NLS_iCre-WPRE-SV40p(A) with retro AAV serotype	VVR ETH Zurich	v148-retro
AAV-8-Ef1a-DIO iC++-EYFP	Stanford Vector Core	GVVC-AAV-108
Chemicals, peptides, and recombinant proteins		
Cholera Toxin Subunit B, Alexa Fluor 488 Conjugate	Invitrogen	C22841
Cholera Toxin Subunit B, Alexa Fluor 647 Conjugate	Invitrogen	C34778
Trimethoprim (TMP)	Sigma-Aldrich	T7883
Experimental models: Organisms/strains		
Mice C57BL/6J	The Jackson Laboratory	JAX 000664
Mice Thy1-GCaMP6f	The Jackson Laboratory	JAX 025393
Mice Ai148(TIT2L-GC6f-ICL-tTA2)-D (also called Ai148D)	The Jackson Laboratory	JAX 030328
Mice Rasgrf2-2A-dCre	The Jackson Laboratory	JAX 022864
Mice Emx1-IRES-Cre	The Jackson Laboratory	JAX 005628
Deposited data		
Original data and code for main figures	This paper	https://doi.org/10.5281/zenodo.7050869
Software and algorithms		
Matlab >R2014b	MathWorks	https://www.mathworks.com/
Suite2p	https://github.com/cortex-lab/Suite2P	Pachitariu et al., 2016
NoRMCorre	https://github.com/flatironinstitute/NoRMCorre	Giovannucci et al., 2018
Fiji / ImageJ	https://imagej.net/software/fiji/	Schindelin et al., 2012
t-Distributed Stochastic Neighbor Embedding (t-SNE)	https://lvdmaaten.github.io/tsne/s	van der Maaten and Hinton, 2008
Motion Mapper	https://github.com/gordonberman/MotionMapper	Berman et al., 2014
SLEAP	https://sleap.ai/	Pereira et al., 2022

RESOURCE AVAILABILITY

Lead contact

Further information and requests for resources and reagents should be directed to and will be fulfilled by the lead contact: Sami El-Boustani (sami.el-boustani@unige.ch).

Materials availability

This study did not generate new unique reagents.

Data and code availability

The complete dataset and Matlab analysis code are freely available at the GERN database, Zenodo, with the doi hyperlink: <https://doi.org/10.5281/zenodo.7050869>.

EXPERIMENTAL MODEL AND SUBJECT DETAILS

All procedures were approved by Swiss Federal Veterinary Office (License number VD1628 and GE15620) and were conducted in accordance with the Swiss guidelines for the use of research animals. Wild-type mice (C57BL/6J) or transgenic mouse lines (mice Thy1-GCaMP6f [C57BL/6J-Tg(Thy1-GCaMP6f)GP5.17Dkim/J, JAX mouse number 025393]; mice Ai148D [Ai148(TIT2L-GC6f-ICL-tTA2)-D, JAX mouse number 030328]; mice Rasgrf2-2A-dCre [B6;129S-Rasgrf2tm1(cre/foIA)Hze/J, JAX mouse number 022864]; mice Emx1-IRES-Cre [B6.129S2-Emx1tm1(cre)Krij/J, JAX mouse number 005628] or the crossing Ai148DxRasgrf2-2A-dCre) were used for experiments. Immune-competent mice were bred in specific pathogen-free facilities before entering experiments. Mice were then housed in ventilated cages with maximum 5 mice in conventional animal facility under a 12/12-h reverse light cycle (light 7 p.m. to 7 a.m.). The ambient temperature in the animal facility was 23°C and the relative humidity was maintained around 50%. Food and water were available *ad libitum* except during behavioral training where water was restricted to 1 mL/day for up to 2 weeks, after which mice had free access to water for at least 2 consecutive days. The cages also contained nesting materials, cardboard house, grids and objects for enrichment. For all experiments, we used adult mice from both sexes and aged between P25 and P300 at the time of the first procedure. Mice used in these experiments were not involved in previous procedures and were test naïve.

METHOD DETAILS

Head plate surgery

All mice first underwent a head implant surgery. Mice were anesthetized with 2–4% isoflurane in pure oxygen. Body temperature was monitored and kept at 37°C throughout the surgery with the help of body temperature-controlled heating pad (DC Temperature Controller, FHC Inc., USA). An eye cream (Viscotears, Alcon, USA; VITA-POS, Pharma Medica AG, Switzerland) was applied over the eyes to prevent them from drying. Carprofen was injected intraperitoneally or subcutaneously (100 µL at 0.5 mg/mL or 100 µL at 1.5 mg/mL) for analgesic treatment before any surgeries. A mix of lidocaine and bupivacaine was injected below the scalp for local anesthetics before opening the skin. In addition, we supplied approximately 0.2 mg/mL ibuprofen (Algifor Dolo Junior, VERFORA Sa, Switzerland) in the cage drinking water for three days after surgery. Once the mouse was anesthetized, we trimmed all whiskers on the right whisker pad except C2 and B2 and head-fixed the mouse on a platform with a nose clamp. Cycles of povidone-iodine solution (Betadine, Mundipharma Medical Company, Bermuda) and 70% ethanol were applied for skin disinfection before surgery. Using surgical scissors, we opened the scalp to expose the skull over the dorsal cortex. We removed all of the connective tissue by scraping the surface of the skull with a scalpel and we spread the temporal muscles by pushing with the side of the blade. Once the skull was cleaned with Ringer solution and fully dried, a custom-made head implant was positioned on top of the skull and glued (Loctite super glue 401, Henkel, Germany) to the right hemisphere of the skull for head-fixation. The head implant was further secured with self-curing denture acrylic (Paladur, Kulzer, Germany; Ortho-Jet, LANG, USA). The surface of the skull was cleared of any denture acrylic to allow optical access for wide-field imaging or optogenetic stimulations. After three days of post-operative care, intrinsic optical signal (IOS) imaging was performed on the left hemisphere as previously described (Sachidhanandam et al., 2013). A piezoelectric actuator was used to repeatedly stimulate either the right C2 whisker or the right B2 whisker. Whiskers were inserted in capillary tubes attached to a piezoelectric actuator that produced continuous 10 Hz pulsatile movements for 4 sec preceded by 4 sec with no stimuli. This was repeated for at least 10 trials with a 10-s interstimulus interval. Increase in absorption (reduced reflectance) of red light at 625 nm upon tactile stimulation indicated the functional location of the C2 or B2 whisker representation in the primary and secondary somatosensory cortices. Throughout the imaging isoflurane was kept around 1% to obtain strong intrinsic responses in somatosensory cortices.

Cranial window surgery for two-photon imaging

For mice used for two-photon calcium imaging, a circular craniotomy with a 3 mm diameter was performed over the primary whisker somatosensory cortex wS1, the secondary whisker somatosensory cortex wS2 or the premotor cortex wM2 (based on stereotaxic coordinates: 2 mm anterior, 1 mm lateral from bregma). Once the bone cap has been removed, the surface of the cortex was rinsed with ringer and the dura was removed using a 27G 1/2 sharp needle bended as a hook. A perfusion system was then used to continuously rinse the surface of the cortex with Ringer and prevent any bloodstain. To express calcium indicators in the areas of interest, adeno-associated viral vectors were then injected in the cortex. A thin glass pipette (PCR Micropipettes 1–10 µL, Drummond Scientific Company, USA) was first pulled and then the tip was broken using a tissue to obtain a 21–27 µm inner tip diameter. The pipette was filled with mineral oil and then tip-filled with the AAV vector. The pipette was lowered to different locations in the brain very slowly and injection was performed using a single-axis oil hydraulic micromanipulator (Narishige, Japan). To express GCaMP6f locally across all cortical layers of wS1 (N = 3 mice) or wS2 (N = 5 mice), AAV1.CamKII0.4.Cre.SV40 was injected in these areas in Ai148D mice. Because this viral vector serotype displays retrograde and trans-synaptic anterograde transduction of the Cre-recombinase (Zingg et al., 2017), the resulting GCaMP6f expression was widespread and uniformly present in all layers. For experiments where wM2-projecting or vOFC-projecting neurons were imaged in wS2, we injected ssAAV-hSyn1-chl-EBFP2_2A-NLS_iCre-WPRE-SV40p (retroAAV.hSyn.eBFP2.Cre) in the target region (wM2 or vOFC) of Ai148D mice (n = 4 mice for wM2-projecting and n = 3 mice for vOFC-projecting). In a different set of experiments, we also injected CAV2-Cre (Hnasko et al., 2006) in these regions in Thy1-GCaMP6f mice together with AAV1.Syn.Flex.NES-jRGECO1a.WRPE.SV40 (Dana et al., 2016) in wS2 to label projecting

neurons with the red calcium indicator jRGECO1a ($n = 4$ mice for wM2-projecting and $n = 3$ for vOFC-projecting). As wM2 could not be identified with intrinsic optical imaging, we used a different approach and took advantage of the retrograde and anterograde trans-synaptic property of AAV1 serotypes (Zingg et al., 2017). For experiments where wM2 neurons were imaged ($N = 3$ mice), we injected AAV1.CamKII0.4.Cre.SV40 in wS2 based on the intrinsic optical signal and injected AAV1.Syn.Flex.NES-jRGECO1a.WRPE.SV40 in wM2 based on stereotaxic coordinates therefore expressing jRGECO1a only in wM2 neurons interacting directly with wS2 either through retrograde or anterograde transduction (Zingg et al., 2017). For all these injections, we injected 50–100 nL at 3 different depths corresponding to deep, intermediate and superficial layers. Injections were done at an approximate rate of 100 nL/min. Once all injections were performed, a sharp razor blade (Wilkinson Sword, UK) mounted on an injection plunger was lowered to the cortex with a micromanipulator (Luigs and Neumann, Germany) to make an incision corresponding to the length of the microprism that will be used to perform two-photon imaging across layers. The blade was lowered slowly in the cortex to a depth of approximately 800 μm . After 3–5 min, the blade was slowly retracted from the cortex. A custom-made microprism window assembly was prepared by gluing a 5 mm round coverslip on top of two co-aligned 3 mm coverslips (CS-3R and CS-5R, Warner Instruments, USA) using UV-curing optical adhesive (NOA61, Thorlabs, USA). A microprism coated with aluminum (MPCH-1.25 for wS1/wS2 and MPCH-1.5 for wM2, Tower Optical Corporation, USA) was then glued to the surface of the 3 mm coverslip in the location corresponding to the incision in the cortex. The microprism window assembly was then held parallel to the craniotomy using a syringe with a flat tip needle attached to a Venturi suction pump. The window was lowered using the same micromanipulator used for the incision and gently placed on the craniotomy while carefully monitoring the insertion of the microprism in the incision. The prism was inserted either in wS1 or wS2 along the medial-lateral axis or in wM2 along the anterior-posterior axis. If any bleeding was caused by the surgery, we waited until they stopped before stopping the rinsing perfusion system. Kwik-Cast sealant or UV-Curing Optical Adhesives (NOA61, Thorlabs, USA) was then applied below the edge of the 5 mm cranial window to protect the cortex. The window was then fixed using super glue and self-curing denture acrylic. Mice were then placed back in their home cage to recover from the surgery. For all these experiments we waited at least 5 weeks for cortical tissues to stabilize before any imaging was performed.

Behavioral training

Mice were trained in a two-whisker go/no go discrimination task under a water-restriction schedule. Mice were head-fixed on a platform and the C2 and B2 whiskers were inserted in capillary tubes glued to piezoelectric actuators mounted in a two-arm holding system with foam to dampen vibration resonance. The tip of the capillary tubes was briefly heated with a Bunsen burner to tighten the opening and better constrain the whisker inside. A plastic sheet was attached below their head on the platform to prevent their forepaws from grabbing the whisker tubes. The piezoelectric actuators were oriented to deliver tactile stimulation along the rostro-caudal axis. A spout was positioned in front of the mouse. A piezo-film was glued to the spout to measure vibration caused by licking activity. Water reward was delivered through the spout using an electronic pinching valve system. The behavior apparatus was controlled with a custom-made user graphical interface based on Matlab (MathWorks, USA) operating a data acquisition card (National Instruments, USA). Each trial started with a quiet window of 2 sec during which any detected lick aborted the current trial. This helped to reduce spontaneous licking and to prevent any lick related signals to contaminate baseline activity prior to tactile stimuli during calcium imaging. Following the quiet window, tactile stimulation could be applied to the C2 whisker, the B2 whisker or none of them. Whisker stimuli consisted of 5 sine waveform pulses, each lasting 40 msec for a total stimulus duration of 200 msec. The amplitude of the tube displacement was ~ 1 mm and was comparable for both whiskers. From stimulus onset, a 2 sec long response window was used to detect licking. Mice were trained to lick the spout in response to the C2 whisker (Go trials) to obtain a drop of water of approximately 8 μL . Licking in response to the B2 whisker (No go trials) resulted in a timeout punishment of 10 sec whereas licking when no stimuli were presented (catch trials) had no consequences on the trial. The proportion of go, no go and catch trials was 30%, 50% and 20% respectively. After the response window, a consumption window of 5 seconds allowed the mouse to collect the water reward. Each trial was therefore 9 sec long and followed by an inter-trial interval of at least 4.5 sec. Before behavioral training started, mice were habituated to head-fixation first for a short duration of about 15 min and then for longer durations. Mice were then trained to the task with one session per day. On the first day of training, mice were exposed to the task with trials where water was automatically delivered following C2 whisker stimulation (Go trials) to engage licking behavior. As soon as they started licking spontaneously, automatic water delivery was stopped and water was only delivered if mice lick for C2 whisker stimulation during the response window. This first phase of training typically lasted for one or two sessions. Mice were then trained daily to the normal task for a period of two to three weeks until they displayed stable behavior as measure by their lick probability for all conditions and discrimination performance. Body weight was monitored daily and was kept above 80% of the weight measured prior to water-restriction. Mice received at least 1 mL of water per day, either during behavioral training or in their home cage. After 14 days of water-restriction schedule, mice were given access to water *ad libitum* for at least 2 consecutive days. In experiments requiring thirst manipulation (Figure 6), we either pre-fed mice with water an hour before the training session or we delayed the session with respect to the normal schedule. In both cases, we monitored body weights after pre-feeding or during the delayed interval to control changes in thirst level while ensuring that weights remained above 80% of reference weight prior to restriction at all time. Pre-feeding and delayed sessions were done in alternance for several consecutive days.

High-speed filming and analysis of orofacial movements

Orofacial movements were filmed at 100 or 200 frames per second using a high-speed camera (CL 600 \times 2/M, Optronis, Germany) under infrared illumination with light outside the visible range of the mouse. The field of view of the camera was oriented and cropped

to capture the face of the mouse and in particular orofacial movements. Movies were monochrome and lasted for the whole trial duration (i.e. 9 sec). Movies of facial movements were analyzed to classify movements using a previously published pipeline Motion Mapper (Berman et al., 2014) based on the dimensionality reduction algorithm t-distributed stochastic neighbor embedding (t-SNE) (Van Der Maaten and Hinton, 2008). After applying principal component analysis decomposition on individual frames, we kept the 50 principal components and ran wavelet decompositions over the temporal domain with 25 frequency bands evenly distributed between 0.5 frames per sec and 30 frames per sec. t-SNE was then applied to the resulting reduced space to obtain two-dimensional maps of orofacial dynamics. Stereotypical movement types were then assigned to each domain of the t-SNE space by inspecting videos extracted during exploration of the domain (see [Video S1](#) for example videos snippets of the stereotypical movements identified). We ran the whole procedure again over all sessions for each mouse to obtain a common map for all sessions. In some cases, this was not possible because the field of view of the camera was changed, in which case individual sessions had their own t-SNE space. In this framework the orofacial movie of each trial is transformed in a trajectory in the t-SNE space defining a sequence of motor states (see [Videos S2](#) and [S3](#) for example videos showing the correspondence between the original movie and the trajectory in t-SNE space for examples of Hit and False Alarm trials). Lick reaction times capturing the very first movement onset time were obtained from this analysis by finding the first time-bin where the trajectory enters (for at least 3 time-bins for robustness) the domain representing licking behavior. Extra spontaneous licking events occurring throughout the duration of the session and their precise timing could also be detected in a similar way (i.e. as stable transitions to the lick domain). In order to collect “isolated” licks the additional constraint of being temporally distant from other lick events was imposed (>0.495 s). This procedure was used to collect spontaneous licking events to better identify motor responsive neurons. Hit trials were not used to recover extra lick events since in this condition late isolated licks could correspond to delayed reward consumption events rather than spontaneous ones. The matrix storing motor state labels for each time bin (columns) of all trial (rows) of a given session is what we defined as an “ethogram” (represented as heatmaps in [Figures 1E](#), [4G–4I](#), and [S1B](#)). The ethogram summarizes the animal motor output in a given session. By summing the number of lick bins (i.e. “isolated licking” and “sustained licking”) after stimulus onset within each trial (along the rows of the matrix) we were able to quantify the duration of licking bouts for each trial throughout sessions.

High-speed filming and analysis of pupil dilation

To establish how thirst-induced motivation affects arousal state we performed pupillometric measurements during task performance. Pupil diameter is a well-established measure of arousal state (Breton-Provencher and Sur, 2019; Vinck et al., 2015). In order to measure pupil area, we filmed the left eye of individual mice at 100 frames per second with high-resolution CMOS camera (Ximea xiQ) equipped with a 6 mm focal length objective (MVL6WA, Thorlabs). Infrared illumination at 940nm was provided by a light-emitting diode array light source (DIR-020-002, Everlight). Recent progress in markerless tracking of body parts based on machine learning approaches have made it possible to reliably monitor changes in high-speed movies (Mathis et al., 2018). Here we used SLEAP deep-learning based pose estimation software (Pereira et al., 2022) to automatically extract markers of pupil contour markers (12 equispaced around the iris contour in steps of 30 degrees as in [Figure 6A](#), with ~500 manually annotated frames from different sessions to train the marker estimation model). The area of pupil polygons defined by SLEAP estimated markers was computed in Matlab for each frame of each video (and expressed in normalized pixel frame-area). All analysis reported in [Figure 6](#) are done associating to each trial the average fractional frame area in the pre-stimulus period. This was done in order to discard stimulus and trial-outcome related pupil signals and slower-timescale arousal fluctuations.

Wide-field imaging

In order to image the dynamics of mesoscale neural activity patterns cross dorsal cortex of mice performing the task GCaMP6f calcium indicator was excited with blue light at 485 nm (halogen lamp, TH4-200 and U-LH100-3, Olympus, Japan; 485/20 BrightLine HC, Semrock, USA) and emission light was detected through a green band pass filter (525/50 BrightLine HC, Semrock, USA). A dichroic mirror (Beamsplitter T 495 LPXR, Chroma Technology Corp, USA) was used to separate excitation and emission light. The left dorsal hemisphere of the cortex was projected on a CMOS chip by using a face-to-face tandem objective (Nikkor 50 mm f/1.2, Nikon, Japan; 50 mm video lens, Navitar, USA). Images were acquired at a resolution of 100x100 pixels (100 μm / pixel) and a frame rate of 100 Hz with a 12 bit camera (MiCAM Ultima, Scimedica, USA). Stimuli and hardware synchronization were done with Matlab using a National Instrument card (NI PCIe-6342) running on a PC. To collect an anatomical reference image for each imaging session, the top of the transparent skull was illuminated with a fiber (M71L02 - \varnothing 1000 μm , 0.48 NA, SMA-SMA Fiber Patch Cable, Thorlabs, USA) coupled to a green LED (530 nm, M530F2, Thorlabs, USA). Movies acquired during behavioral sessions were processed after the experiments. For each trial, we computed a baseline image as the average of the last 5 frames prior to the stimulus onset. This baseline image was used to compute a relative change in fluorescence for the rest of the trial following response window onset. This was done by subtracting the baseline image from each frame and then dividing the resulting image with that same baseline. The image of the skull taken with green light was used to identify Bregma and delimit the edge of the skull. For each mouse, we collected trials from several sessions (between 5 and 10) to compute an average response map for each trial condition with large numbers of trials. For mice expressing GCaMP6f in cortical layer 2/3 (Ai148DxRasgrf2-2A-dCre), we registered maps across mice using the peak response in wS1 for C2 whisker stimulation. This is a highly reliable functional landmark and we confirmed that all response maps aligned properly after registration. Bregma was measured for each mouse based on the skull image and the mean location for the anatomical landmark is displayed in the figures. To express GCaMP6f in wM2-projecting neurons, we injected wM2 of Ai148 Cre-dependent GCaMP6f

reporter mice with retroAAV.hSyn.eBFP2.Cre viral vector to express Cre-recombinase in wM2-projecting neurons across the dorsal cortex. For these mice, we registered maps across mice using Bregma as the functional responses during passive whisker stimuli were much weaker. Once all cortices were aligned across mice, we compared responses between lick and no-lick conditions for both C2 and B2 whisker stimulation. A one-sided paired t-test was applied for each pixel to compare these conditions for all mice. The time window chosen to compute and compare maps for lick and no-lick conditions was the last 60 msec before lick-evoked widespread activity. The normalized difference between average responses was computed as the difference between the response in lick condition and the one in no-lick condition divided by the sum of these two.

Perfusion and postmortem analysis

Mice that received injections of viral vectors, CTB-Alexa488 or CTB-Alexa647 were euthanized for postmortem analysis. After being deeply anesthetized with 4% isoflurane, they were overdosed with pentobarbital injected intraperitoneally. After perfusion with approximately 25 mL of PBS (0.9% NaCl, 0.01M phosphate buffer, pH 7.4), they were then perfused with 25 mL of 4% paraformaldehyde (PFA). The brains were then extracted from the skull and kept in 4% PFA overnight and then transferred into PBS. Brain coronal sections were then cut using a vibratome (Leica VT1200S) and imaged using an epifluorescence microscope (Olympus Slide Scanner VS120-L100 or LEICA DM 5500) through a 10x/0.40 NA air objective.

Optogenetics

Optogenetics silencing experiments were performed using Emx1-IRES-Cre mice injected with AAV-8-Ef1a-DIO iC++-EYFP in specific cortical regions. This opsin responds to blue light by hyperpolarizing membrane potential and was used to silence Emx1-positive excitatory neurons in the cortex. For experiments involving inactivation of wS1, wS2 or wM2, a 1 mm diameter optic fiber attached to a 470 nm high power laser (MBL-F-473/200 mW, Changchun New Industries Optoelectronics Technology, China) was used to deliver blue light at the surface of the cortex through the glue covered skull. The fiber was positioned with a micro-manipulator and placed over the area to be silenced. For experiments involving inactivation of the orbitofrontal cortex, a fiber optic cannula with 400 μ m diameter (CFMLC14L02, Thorlabs, USA) was inserted in the cortex after injection of AAV-8-Ef1a-DIO iC++-EYFP using the same penetration track. To target vOFC without going through wM2 we used the following coordinates after tilting the brain 30 degrees to flatten the surface of the cortex over vOFC: 2 mm lateral, 2 mm anterior and 2.3 mm deep from bregma. The cannula was then attached to the skull using super glue and self-curing denture acrylic. During behavioral training the cannula was coupled to the laser fiber using a ceramic mating sleeve. The location of the expression site and the position of the fiber over the ventral orbitofrontal cortex were confirmed with post-mortem analysis. During the whisker discrimination task, blue light stimulation was delivered in 50% of trials interleaved with control trials and consisted of continuous illumination at approximately 10 mW/mm² starting 100 msec before stimulus onset and lasting for 1 sec after stimulus onset. Change in lick probability was measured during blue light illumination in the response window. To ensure that mice did not directly perceive the blue light used for optogenetic silencing, we displayed a strong masking blue light in front of the mouse and isolated with an opaque sleeve the fiber on top of the skull. To better assess the contribution of each cortical area in the execution of the task, we used single whisker deflection at moderate amplitude.

Two-photon imaging

A custom made two-photon microscope was used to perform calcium imaging experiments described in this paper. The microscope was equipped with a galvo-resonant mirror pair (8 kHz CRS, Cambridge Technology, USA), allowing a frame rate of 30 Hz for resolutions of either 512 \times 512 pixels or 512 \times 1024 pixels with the frame length being along the resonant scanner axis. A femtosecond tunable infrared laser line (Mai Tai or InSight DeepSee, Spectra Physics—Newport, USA) was fed into the light path at a wavelength of 940 nm or 1000 nm to excite the genetically encoded calcium indicator GCaMP6f or jRGECO1a respectively. Light emission was detected with a GaAsP photosensor module (H10770PA-40, Hamamatsu, Japan), and signal acquisition was performed with National Instrument hardware (NI PXIe-1073, NI PXIe-6341, National Instruments, USA). The microscope head was movable and controlled in three dimensions by motors (Luigs and Neumann, Germany). A 16x immersion objective (16x Nikon CFI LWD, Japan) was used for all the imaging. The system was operated by the Matlab-based software ScanImage SI5 (Vidrio Technologies, USA). For each mouse, multiple imaging sessions were performed at very different depths and locations within the field of view in the micro-prism. During the behavior sessions, we used a trial-based acquisition scheme where acquisition sequences of fixed duration (9 sec) were triggered at the beginning of each trial.

Two-photon calcium data pre-processing

To extract time-varying somatic calcium signals, we used the Matlab-based Suite2p toolbox (Pachitariu et al., 2016). Neuropil contamination was corrected by subtracting the fluorescent signal from a surrounding ring $F_{\text{Surround}}(t)$ from somatic fluorescence: $F(t) = F_{\text{Soma}}(t) - \alpha \cdot F_{\text{Surround}}(t)$, where α was estimated by the Suite2p deconvolution algorithm. Neuropil-corrected fluorescence signals $F(t)$ were then converted in z score by subtracting from each trace the mean value and dividing by its standard deviation of $F(t)$ over the samples contained in the last second of the baseline window preceding the stimulus (pooling across all trials).

Behavioral analysis and state classification

We observed the behavior of mice performing the task transitioning across 4 stereotypical behavioral patterns as their thirst-induced motivation decreased over the course of each session. This analysis was based on the lick probability for all stimulus conditions (C2 whisker, B2 whisker, No stimulus) as well as the discrimination performance measured as the percentage of correct trials. We labeled the first stage “hyper-motivated” (gray shaded areas in Figures 5A and S5A). In this state mice produced many spontaneous licks (i.e. licks not evoked by a whisker stimulation) and tend to lick indiscriminately upon stimulation of any whisker. We labeled the second state as “detecting” (brown shaded areas in Figures 5A and S5A). In this state, the motivation starts to decrease and mice stop licking when not cued by a whisker stimulation but they remain unable to suppress licking for the No go whisker (B2). We labeled the third state as “discriminating” (green shaded areas in Figures 5A and S5A). In this state, mice finally stop licking for the No go (B2) stimulus while continuing to lick upon stimulations of the Go whisker (C2). The last state was labeled “disengaged” (white areas in Figures 5A and S5A). In this state, the motivation becomes so low that mice eventually stop licking for any stimulus, even upon stimulation of the Go whisker (C2). Figure S5A illustrates the sequence of states described above in an idealized case. In order to automatically label trials as belonging to one of these 4 states we implemented a behavioral data analysis pipeline that is schematically depicted in Figure S5B. We first isolated each stimulus condition (C2, B2, No stim.) during the session to compute a smoothed lick probabilities over a sliding window of 61 consecutive trials. This is computed as the number of licks in a stimulus condition divided by the number of occurrences of that given condition in the sliding window. From these condition-specific smooth lick probabilities, we also computed a performance variable as the percentage of correct trials. It is defined as the average between the rate of correct choices for C2 whisker stimulations (i.e. Hit rate = C2 lick rate) and the rate of correct choices for B2 whisker stimulations (i.e. Correct Reject rate = 1 – False Alarm rate = 1 – B2 lick rate). These curves are the ones displayed in Figures 5A and S5. This way of computing performance makes it insensitive to the proportion of C2 vs. B2 trials. We chose to use this performance metric rather than the signal detection d' to avoid the divergence problem for low-variance distributions that were often observed in our data when hit rate was stuck at 1. However, additional analysis with a regularized version of d' showed similar results as the one reported in this study (data not shown). The next step is a first labeling of each trial as belonging to one of the 4 possible states depending just on the local values of the above-mentioned curves. The decision tree describing the logic of this labeling is depicted in Figure S5B. In the following we provide a brief summary of this process. First trials in which spontaneous lick probability exceeds a threshold value of 0.3 are labeled as “hyper-motivated”. Next remaining trials are labeled as “detecting” if at least one of the two stimulus evoked lick probabilities (i.e. C2 and B2) exceeds the threshold value of 0.3 and the C2-evoked one is not exceeding the B2-evoked one above a given threshold of 0.2. On the contrary, if this latter condition is met, the trial receives the label of “discriminating”. Remaining trials are labeled as disengaged. This procedure already yields a relatively good match with the intuition described above in the majority of sessions, however this kind of “threshold crossing” algorithm is prone to noise around state transitions (producing a multitude of very small chunks of trials with alternating labels when the lick probabilities randomly fluctuate around the threshold values). In order to fix this problem and make sure sessions are always chunked in a sequence of large state phases (likely to be more behaviorally relevant in reflecting the change of motivational state of the animal) we applied two extra post-processing steps. The first is the application of a “gap filling” algorithm to the sequence of behavioral state labels of each session. The algorithm is composed of three main steps: i) the state sequence is padded with “hyper-motivated” and “disengaged” at the beginning and end respectively; ii) for each isolated chunk of length <50 in the sequence we take a window of width 100 centered in its middle point and we replace current label with one that is more abundant in the neighboring bins; iii) a session “end point” is detected as the trial, after peak performance has been reached, in which the curve goes under 0.66 of the peak performance: every trial after this point is re-labeled as disengaged and padding is removed. Finally, as a second post-processing step, sequential ordering (‘hyper-motivated’->‘detecting’->‘discriminating’->‘disengaged’) of the remaining chunks is ensured by filling up remaining isolated chunks with the label of the earliest state not terminated yet for the current session (where termination is defined as the trial in which the last label of a given state appears in each particular session). In order to assess the learning of each individual mouse, we computed a session-by-session C2 vs. B2 discrimination performance including only “engaged” trials (i.e. hyper-motivated + detecting + discriminating). By performing a bootstrap-t procedure resampling over trials we obtained p-values for this difference in each session. Displaying at least one session with significantly positive C2 vs. B2 lick rate difference was adopted as criterion for learning. In order to quantitatively assess how fast mice improved their task performance over days we computed learning curves by averaging performance session-by-session and considering all engaged trials. For each mouse, after a mild smoothing of the learning curves (i.e. moving average with window of length = 5) we defined as “sessions to criterion” the number of sessions required for these smoothed performance curves to reach 75% of the peak value. To quantify performance improvement within the discriminating state across sessions we re-applied exactly the same procedure to session-by-session performance curves obtained only considering “discriminating” states. Another important metric of progression of mice proficiency in the task we computed is the fraction of trials spent in the “discriminating” state over the total number of “engaged” trials of each session (Figure 5F).

Simulations of learning trajectories

We simulated two distinct learning scenarios to illustrate how the behavioral state analysis can distinguish between them and characterize how mice performance progressed across days. We considered a “sensorimotor learning” scenario and a “motivational state control” scenario and we simulated the outcomes of the analysis in the two cases. For both scenarios we implemented a toy model able to generate synthetic behavioral data following specific changes in behavioral curves. Single trial licking events

were drawn from a binomial probability distribution controlled by the lick probability curves. These simulated data were then fed to the same analysis pipeline used for real data (Figure 5). In the first scenario (“sensorimotor learning”) performance increase is driven by a linear increase of the gap between the C2 and B2 lick probability plateau levels across sessions. Session after session C2 lick probability remains fixed at 1 while B2 lick probability linearly decreases (downward red arrow in Figure S5C). This yields a flat performance curve within each session steadily increasing across days (upward blue arrow in Figure S5C). This scenario mimics the hypothetical case of a mouse slowly strengthening the sensorimotor association between whisker stimuli and actions while expressing this knowledge at all times during the session. In the second scenario (“motivational state control”) performance increase is driven by an increase of the duration of the discriminating phase in each session with the B2 lick probability decaying to zero progressively earlier before the C2 one lick probability curve (leftward red arrow in Figure S5I). This results in an inverted U-shaped performance curve with broader and broader peak across days (upward blue arrow in Figure S5I). This scenario mimics the hypothetical case of a mouse that has acquired the sensorimotor association early but is not able to express this latent knowledge at all times during training. On the contrary task knowledge expression in this scenario can happen only during a final discrimination phase that progressively increase in duration as the animal learns to control its motivational state across days. To compare the results of these simulations with real data we quantified in both cases the slopes of the discriminating phase proportion and discriminating performance curves over late sessions close to the saturation point of the sigmoidal learning curve (Figures S5H and S5N). The same process was repeated for different discrimination thresholds (i.e. minimal C2 vs B2 lick rate difference) used by the behavioral phase classification algorithm to ensure robustness to the choice of this parameter.

Classification of neurons in functional cell classes

Whether a neuron was responsive to each condition (“Hit”, “Miss”, “False Alarm”, “Correct Rejection” and “Catch”, including all spontaneous licking events realigned to licking time) was assessed by performing a one-sided unpaired z test on the z scored calcium traces for each trial time bin. Bins for which the distribution of z scored activity was exceeding a threshold of significance of $p < 10^{-10}$ for at least 3 consecutive bins were considered a “responsive” bin. A neuron having at least 1 responsive time bin in a given condition was considered “responsive” to that condition. Whether the calcium responses of a neuron were better aligned to the onset time of licking movements or to the onset of whisker stimulation was assessed by performing a two-sided paired t-test comparing the mean value of peak z scored calcium traces (in Hit and False Alarm conditions) keeping trials aligned to stimulus (stimulus-aligned) vs. aligned to lick timing (lick-aligned). A neuron having an average response peak significantly greater (i.e. with $p < 0.05$) in the lick-aligned condition than in the stimulus-aligned condition was considered “motor aligned”. Responsive neurons were assigned to 4 different functional cell classes (i.e. “pure sensory”, “mixed sensory”, “gated sensory” and “motor-related”). The decision tree used for the cell classification algorithm is depicted as flowchart in Figure S4A. In the following we will briefly summarize the logic of the classification. i) If a neuron is responsive only in presence of one or both sensory stimuli (i.e. to Hit & Miss or False Alarm & Correct Reject) and not motor-aligned we will consider this cell a “pure sensory” neuron since it responds to sensory events only. ii) If a neuron is responsive to one or both sensory stimuli (as in the previous case) but also to spontaneous licking events or if its responses are motor-aligned we will consider this cell a “mixed sensory” neuron since it responds to both sensory and motor events. iii) If a neuron is unresponsive to any sensory stimulus alone as well as to spontaneous licks but is responsive to whisker stimuli in lick conditions (i.e. Hit or False Alarm) while not being motor-aligned we will consider this cell as “gated sensory” neuron since it responds as a sensory neuron but only when the stimulus is followed by the action to lick (i.e. the lick decision “gates” the sensory response). iv) If a neuron is unresponsive to any whisker sensory stimulus alone as well as to spontaneous licks but is responsive to catch or its responses are lick-aligned we will consider this cell a “motor-related” neuron since it responds to motor events only.

Quantification of whisker selectivity

In order to quantify the sensory selectivity of imaged neurons we computed a “whisker selectivity index” (WSI) characterizing the difference between responses to C2 whisker and B2 whisker in No lick trials (to avoid any confounding effects due to motor-related signals potentially present in Lick trials). The first step in computing WSI consists in taking Miss and Correct Reject trial responses and baseline correct them (by subtracting the median of the traces in each condition between -2 and -0.5 from stimulus onset to the traces themselves). Next, traces of each trial are integrated over the whole response window (i.e. between 0 and 2 sec after stimulus onset). Finally, WSI value is given by taking a normalized difference between the average across trials of these integrals for the Miss and Correct Reject condition (leading to positive values for neurons preferring the C2 whiskers and negative values for neurons preferring B2). In the histogram in Figure 3G neurons referred as whisker selective are neurons with $\text{abs}(\text{WSI}) > 0.33$. When computing WSI by behavioral state the same logic applies but this time all C2 and B2 trials are considered since motor-related and mixed sensory neurons are excluded from this analysis (therefore excluding contaminations with motor-related signals). Average WSI curves shown in Figure 7C are obtained by averaging these WSI values by behavioral state including, for each state, only cells for which >10 trials have been observed for both whiskers in that particular state (to ensure good sampling). Average z scored amplitude curves shown in Figure 7D are obtained by taking the average between the max C2 and B2 z score responses of the same signals from which WSI is computed and averaging, for each state, only over cells for which >10 trials have been observed for both whiskers.

Quantification of pre-lick modulation in sensory responses

In order to quantify modulations of sensory responses by the upcoming action (i.e. lick or no lick) we devised a “pre-lick modulation index” (PMI) that compares, trial-by-trial observed responses in the Stim + Lick condition (i.e. Hit or False Alarm) with the one predicted looking at the average of the Stim + No lick condition over a time window preceding lick time in each trial. [Figure S4C](#) displays a schematic showing how the PMI is computed for an example pure sensory neuron. In the following we will briefly summarize the steps of the algorithm to compute this index. The first step consists in computing the trial average of the response in the Stim + No lick condition (after a baseline correction step in which the median of the trace between -2 and -0.5 sec from stimulus onset is subtracted to the traces). Next the algorithm requires to loop over trials in the Stim + Lick condition and for each of them define a “pre-lick window” as the time between stimulus onset and one time bin (i.e. 33 msec) of margin before the t-SNE estimated lick time. The current Stim + Lick trial z scored response and the average z scored one in the Stim + No lick condition have to be integrated over this time window to produce two response integrals (indicated as “i1” and “i2” in [Figure S4C](#)). To reduce the noise in the estimate of these two integrals, time samples not crossing a significance threshold of $p < 10^{-10}$ (i.e. “unresponsive” bins) for both the Stim + Lick and Stim + No Lick conditions are excluded from the integration as well as the ones for which a pre-lick response was observed for less than 5 trials (i.e. “undersampled” bins). The PMI value is finally obtained by taking a normalized difference between the averages across Stim + Lick trials of i2 and i1 (resulting in a positive value for an enhancement of the responses preceding licks and negative values for a depression).

Clustering of populations according to similarities in pre-lick modulation

In order to find the best clustering of neural populations under investigation according to the similarity of their PMI values we applied hierarchical clustering approach. The hierarchical clustering algorithm (implemented in Matlab Statistics and Machine Learning Toolbox™) was fed with the surprise matrix derived from p values obtained from a two-sided paired Wilcoxon test comparing the median C2 and B2 PMI values of each pair of populations. The linkage to be fed to Matlab function “dendrogram” (outputting the reordering permutation) was created using the “average” method and “cosine” metric. The matrix of surprise values for median PMI differences was then reordered applying the permutation minimizing clustering distance between rows and columns to obtain the result shown in [Figure 3K](#).

Analysis of action tuning maps

Action tuning maps were characterized in the t-SNE space by computing the ratio between the unweighted trajectory-occupancy histogram and the one obtained weighting each position with neuronal activity recorded during transit of the trajectory in that particular bin. Histograms were filtered with a gaussian kernel before taking the ratio to get smoother tuning maps. For this analysis we used z scored deconvolved calcium traces as representation of neuronal activity. This choice was dictated by the need to avoid the potential smearing of the reconstructed tuning map along the trajectory due to the long tail of the calcium fluorescence signal. Z scoring of deconvolved trajectories was carried out following the same procedure described above for fluorescence traces. In order to investigate in which state of the typical trajectory in t-SNE space any neuron would fire (i.e. to understand which point of the typical motor sequence each neuron encodes) we devised a “convolved trajectory analysis” based on the idea of convolving the action tuning map with the typical motor trajectory. The first step of this analysis was to reparametrize trajectories in the t-SNE space with an intrinsic length coordinate thus making them insensitive to small trial-to-trial variation in the exact dwelling time in any given region. In doing so only the part of the trajectory going from the exit to the entrance in the quiet state was considered to discount the effects of different reaction times and overall motor sequence duration. In order to obtain such a reparameterization we devised an algorithm that “jumps” from point to point (potentially skipping groove points) along the original trajectory. The algorithm selects the destination of the “jump” (i.e. the next point in the reparametrized trajectory) weighting different factors: i) the distance in t-SNE space of next candidate points from the current one (trying to match an ideal reparameterization step size), ii) their angular distance with respect to the current direction of the trajectory (trying to deviate as little as possible), iii) the distance in time samples of next candidate points from the current one (to avoid big “jumps”). After a final interpolation step the reparametrized single-trial trajectories obtained in this way are summarized in a typical trajectory by taking their mode point-by-point (the mode is obtained by taking the maximum density point of the estimated distribution of positions of the reparametrized trajectories for all values of the intrinsic coordinate). Having obtained these typical reparametrized trajectories for each session the next step consists in convolving them with the tuning map of each motor neuron recorded in that session. This yields a “convolved trajectory trace” for each neuron where the peak represents the preferred stage of the motor sequence for each cell (black dots in [Figure 4E](#)). Averaging across all motor neurons (after a max normalization step) from all sessions recorded in a given area yields the curves visualized in [Figure 4E](#) describing where, along the motor sequence, the majority of motor neurons are active in wS1, wS2 and wM2.

Decoding the identity of the stimulated whisker

In order to quantify the amount of information about the tactile stimulus encoded in different areas and across different behavioral states we implemented a decoder classifying trials as “C2 stimulation” or “B2 stimulation” on the basis of neuronal population activity of neurons in each session. This decoder was inspired by original works introducing neuronal population probabilistic codes ([Jazayeri and Movshon, 2006](#); [Ma et al., 2006](#)) and is similar to the one used in a previous publication ([Mayrhofer et al., 2019](#)). The first preparatory step for this analysis was to compute, for all non-motor neurons in a given session (i.e. “pure sensory” and

“gated sensory”) the integral of the z scored responses over the whole response window on each C2 or B2 trial. This yielded a dataset amenable to be solved as a binary classification problem: for each trial, we have a population “feature vector” containing the response integral of all neurons in the population and a “label vector” encoding the identity of the whisker being stimulated at that time. To solve this classification problem with the probabilistic approach mentioned above while ensuring robustness of the results we applied a 4-fold cross-validated procedure in which we split trials of any given session in 4 batches and we used 3 of them for “training” of the decoder and 1 for “testing” (i.e. to evaluate the decoding performance on hold out data). The “training” in this probabilistic framework consists simply in computing the tuning curves (i.e. whisker-triggered averages) using all trials included in the training set and taking their logarithm. The subsequent “testing” of the decoder requires to generate a prediction. This is done by computing the log-likelihood of test trials being fed as a C2 trial or a B2 trial and selecting as predicted whisker the maximum likelihood one. The log-likelihood can be obtained by taking a matrix product between the matrix storing the log of tuning curves computed at the “training” step and the current population feature vector (after subtracting a corrective term proportional to the sum of all tuning curves to account for any representational bias in the decoded population). The fraction of correct predictions (i.e. when the predicted whisker coincides with the true one) is the accuracy of the decoder on the test set. The average test set accuracy across each of the 4 train/test splits was used to measure the decoding performance in a given session. This process was repeated 250 times reshuffling the neurons to make sure the results were fully independent from any particular train/test split. As a preprocessing step, each element of the population feature vector was scaled independently between 0 and 1 and the order of trials was randomly reshuffled (while keeping the correspondence with the correct label) in order to get rid of noise correlations. To obtain curves of accuracy vs. number of neurons in the decoded population in [Figure 7E](#) the process described above was repeated subsampling the neuronal population to match a given neuron number for all neuron numbers from 1 to the total number of neurons recorded in each session. Performance curves obtained in this way were then averaged across all sessions recorded in each area. The same procedure was applied limiting trials to only the ones in a given state in order to obtain decoding performances per behavioral state (using all neurons in each session). These performances were in turn used to compute the performance variation in each state relative to the average across states. This normalized performance variation was indicated as “ Δ Decoding performance” in [Figures 7F–7H](#). The same procedure was followed for the results in [Figure 7G](#) where an additional resampling procedure generating “surrogate” sessions was applied (see Statistics section below for the details). All plots in [Figure 7](#) showing decoding performances include only sessions with at least >20 trials observed for both C2 and B2 (i.e. “well-sampled sessions”).

Decoding orofacial movements

In order to quantify the amount of information about orofacial movements encoded in different areas we implemented a decoder classifying each bin of each trial as pertaining to one of the 7 possible motor states on the basis of neuronal population activity of neurons in each session. As for the whisker decoder this decoder was also inspired by population probabilistic codes ([Jazayeri and Movshon, 2006](#); [Ma et al., 2006](#)) and similar to the one used in a previous publication to decode left vs. right licks from tongue-jaw M1 and wS1 activity ([Mayrhofer et al., 2019](#)). However, the higher dimensional nature of the problem, as compared with whisker decoding, required several adaptations. In this case our probabilistic decoder was not trying to directly predict the state label for each time bin but rather the position in the t-SNE state space. Boundaries of regions associated to different motor states in the t-SNE space provided the link function to translate these predicted positions in predicted state labels. The first preparatory step for this analysis was to extract the value of smoothed deconvolved activity traces in the time interval from -1 to 6 sec after stimulus onset for all non-sensory neurons in a given session (i.e. “motor-related” only). Smoothing was carried out by convolving raw deconvolved traces with a causal exponential filter with $\tau = 0.230$ sec. This yielded a dataset amenable to be solved as a multi-class classification problem: for each time sample of each trial, we have a population “feature vector” containing the response integral of all neurons in the population of interest and a “t-SNE position vector” encoding the position in the t-SNE plane that time (encoded by an integer number between 1 and 500). To solve this problem with our probabilistic approach while ensuring robustness of the results we applied a 3-fold cross-validated procedure in which we split trials of any given session in 3 batches and we used 2 of them for “training” of the decoder and 1 for “testing” (i.e. to evaluate the decoding performance on hold out data). The “training” of our probabilistic framework consists simply in computing the action tuning map for each neuron (i.e. tuning curves in the t-SNE space, as described in detail in the Analysis of action tuning maps section) using all samples of all trials included in the training set and taking their logarithm. The subsequent “testing” of the decoder requires the generation of a prediction. This is done by computing the log-likelihood of the test time sample being fed as input corresponding to any point of the t-SNE space and selecting as predicted position the maximum log-likelihood one. The log-likelihood can be obtained by taking a matrix product between the matrix storing the log of tuning curves computed at the “training” step and the current population feature vector (after subtracting a corrective term proportional to the sum of all tuning curves to account for any representational bias in the decoded population). As mentioned before, the position predicted in this way is translated in a predicted state using the known state boundaries. As a preprocessing step, each element of the population feature vector was scaled independently between 0 and 1 and the order of trials was randomly reshuffled (while keeping the correspondence with the correct label) in order to get rid of noise correlations. Repeating the procedure described above we can get a state prediction for all time samples of all trials of a session. We can then visualize these data as a predicted ethogram that we can compare with the true one (as in [Figures 4G–4I](#)). The fraction of correct predictions across all time bins of all testing trials (i.e. the fraction of times over which the predicted motor state label coincides with the true one) is the accuracy of the decoder on the test set. The average test set accuracy across each of the 3 train/test splits was used to measure the decoding performance in a given

session. For the results reported in [Figure 4J](#) only “active” time samples (defined as moments in which at least one neuron in the population feature vector was above its 25% quantile of activity) were taken in consideration to limit the assessment of performance to moments in which some activity was present in the motor network imaged. Predicted ethograms were also used to decode lick bout duration in each trial by integrating the time spent in “isolated licking” and “sustained licking” in each trial. Agreement between predicted and observed lick bout duration in each session was quantified as the Pearson correlation coefficient between these 2 variables. Prediction of ethograms can also be achieved using a more standard Generalized Linear Models (GLM) approach based on neuronal activity to predict moment-by-moment discrete behavioral states. Performing the same analysis using GLM models we found a similar trend as the one observed with Bayesian decoder for different areas with an overall lower fraction of correct trials (data not shown).

Quantification and statistical analysis

Statistical details of experiments and analysis are described in figure legends and in the Results section. Details include statistical tests used, sample type and number as well as definition of bar plots and error bars. In figure legends, standard error of the mean (s.e.m.) is specified when plotted as error bars. Paired or unpaired t-tests were used to assess significance of mean comparisons (implemented by Matlab functions “ttest” and “ttest2” respectively). Normality tests were not performed systematically but individual data points were plotted to visualize distributions. Wilcoxon signed rank test were used to assess significance in paired median comparisons (implemented by Matlab function “signrank”). Wilcoxon rank sum test was used for unpaired median comparisons (implemented by Matlab function “ranksum”). Pearson correlation coefficient was used to compute correlations between two conditions (implemented by Matlab function “corr”). Across all fits reported uncertainties (i.e. confidence intervals) for best-fit parameter values were extracted fit covariance matrices (fitting was performed using Matlab function “nlinfit”). When comparing systematically many populations (>3, like in the analysis described in [Figures 3K](#), [6F–6G](#), and [7G](#)) Bonferroni multiple comparison correction was applied. Custom bootstrap or resampling procedures were adopted when in need of applying particular constraints to the distributions to be compared (i) or when the complex nature of the analysis involved was making them less amenable to a more standard approach (ii, iii, iv). In the following lines we will outline the procedures adopted in these cases more in detail. i) When comparing PMI values across sensory neurons (i.e. “pure sensory”, “mixed sensory” and “gated sensory”) in each neuronal population as a function of the whisker identity ([Figure 3H](#)) a bootstrap procedure with sample size matching was applied. This was important to discount from the comparison any effect of the differences in overall whisker preference between areas. Neurons were resampled 2,000 times subsampling every time the largest population among the C2 preferring (i.e. $WSI > 0$) and the B2 preferring (i.e. $WSI < 0$) to achieve equal sampling (i.e. $wS1: n = 366$, $wS2: n = 392$, $wM2: n = 293$). The average across neurons for the C2 and B2 PMI as well as their difference was then computed for each resampling. Finally, the distribution thus obtained was used, under a normal assumption, to compute Z values and compute the corresponding p value for the difference from zero as well as 95% CI. ii) When comparing the results of the convolved trajectory analysis across areas a bootstrap-t procedure ([Efron and Tibshirani, 1993](#)) with 2,000 outer resamplings and 25 inner resamplings (over neurons) was applied in order to obtain 95% CI for the mode of the distribution of peak positions of the convolved trajectory traces. iii) When comparing whisker Δ Decoding performances across behavioral states ([Figure 7G](#)) it was important to compare average performance between sessions containing both states in the pair under consideration only (e.g. when comparing “discrimination” and “disengaged” only sessions featuring these two states with a sufficient number of trials per whisker should be included). In order to be able to do so while still keeping a good number of samples for the comparison we resorted to a resampling approach in which we created n surrogate sessions from each session with n neurons. This enabled to keep the number of samples high enough (greater than >14 in the worst case) to have a meaningful comparison for all pairs of states. iv) When assessing the difference from zero of the C2 vs. B2 lick rate difference in each session of each mouse a bootstrap-t procedure ([Efron and Tibshirani, 1993](#)) with 2,000 outer resamplings (over trials) and 25 inner resamplings was applied in order to obtain 95% CI.